Kidney disease reprograms microbiome-host signaling to promote heart failure

Alex Yarritu[1,2,3,4,*], Wibke Anders[1,2,3,4,5,*], Arne Thiele[1,2,3,4], Olena Potapenko[1,2,3,4], Fabian Schumacher[5], István A. Szijártó[1,2,3,4], Ariana Matz-Rauch[1,2,3,4], Jakob Versnjak[6], Natnael Gebremedhin[1,2,3,4], Victoria McParland[1,2,3,4], Simon Heckscher[7], Sakshi Kamboj[7], Giuseppe Trimarchi[3,8], Harithaa Anandakumar[1,2,3,4], Franziska Fuckert[1,2,3,4], Carina Hoffmann[1], Sara A. Hassan[1,5], Paul M. Bonnekoh[1,2,3,4], Moritz I. Wimmer[1,2,3,4], Felix Behrens[1,2,3,4], Jakob Voelkl[3,4,9], Rafael Kramann[10], Ulrich Kintscher[3,8], Titus Kuehne[3,6,11], Burkhard Kleuser[5], Alma Zernecke[12], Peter J. Oefner[7], Wolfram Gronwald[7], Katja Dettmer[7], Kai-Uwe Eckardt[4], Dominik N. Müller[1,2,3,13], Marcus Kelm[3,6,11], Johannes Holle[1,2,3,14], Hendrik Bartolomaeus[2,3,12,†], Nicola Wilck[1,2,3,4,†]

[1]Experimental and Clinical Research Center (ECRC), a cooperation of Charité – Universitätsmedizin Berlin and Max Delbrück Center for Molecular Medicine, Berlin, Germany

[2]Max-Delbrück-Center for Molecular Medicine in the Helmholtz Association, Berlin, Germany

[3]DZHK (German Centre for Cardiovascular Research), partner site Berlin, Germany.

[4]Department of Nephrology and Medical Intensive Care, Charité – Universitätsmedizin Berlin, corporate member of Freie Universität Berlin and Humboldt-Universität zu Berlin, Berlin, Germany

[5]Freie Universität Berlin, Department of Biology, Chemistry and Pharmacy, Institute of Pharmacy, Berlin, Germany

[6]Institute of Computer-assisted Cardiovascular Medicine, Deutsches Herzzentrum der Charité, Berlin, Germany

[7]Institute of Functional Genomics, University of Regensburg, Regensburg, Germany

[8]Max Rubner Center for Cardiovascular Metabolic Renal Research, Institute of Pharmacology, Charité – Universitätsmedizin Berlin, Berlin, Germany

[9]Institute for Physiology and Pathophysiology, Johannes Kepler University of Linz, Linz, Austria

[10]Division of Nephrology and Clinical Immunology, University Hospital RWTH Aachen, Aachen, Germany
[11]Department of Congenital Heart Disease – Pediatric Cardiology, Deutsches Herzzentrum der Charité, Berlin, Germany
[12]Institute of Experimental Biomedicine, University Hospital Würzburg, Würzburg, Germany
[13]Charité – Universitätsmedizin Berlin, corporate member of Freie Universität Berlin and Humboldt-Universität zu Berlin, Berlin, Germany
[14]Department of General Pediatrics and Hematology/Oncology, University Children's Hospital, University Hospital Tübingen, Tübingen, Germany
*These authors contributed equally to this work.
†These authors contributed equally to this work.
Correspondence: nicola.wilck@charite.de

Summary

Gut microbiome-derived metabolites regulate host physiology, with systemic levels controlled by renal excretion. In kidney disease, impaired clearance leads to metabolite accumulation, inflammation, and secondary cardiovascular damage. We show that adverse cardiac remodeling following kidney disease critically depends on the microbiome. We identify microbiome-derived indoxyl sulfate-mediated activation of the aryl hydrocarbon receptor (AhR) as a key mechanism inducing IL-17A-producing T cells, thereby promoting cardiac fibrosis. AhR inhibition attenuates inflammation and cardiac remodeling. On population level, IL-17A is elevated in chronic kidney disease, particularly with coexisting heart failure. Mechanistically, AhR and IL-17A signaling induce a conserved pro-fibrotic phenotype in both murine and human cardiac fibroblasts. This work identifies a microbiome-AhR-IL-17A axis as a mediator and druggable target of cardiovascular damage in kidney disease.

Introduction

Multimorbidity, the coexistence of two or more chronic conditions, is a major challenge for future medicine[1]. Secondary organ damage arises from a complex interplay between intrinsic physiological processes and environmental exposures. The crosstalk between the kidney, a key regulator of internal homeostasis, and the gut microbiome[2], a metabolically active interface between host and environment is particularly relevant. Chronic kidney disease (CKD), a growing global health burden[3], impairs the clearance of host- and microbiome-derived metabolites, leading to their accumulation and toxic effects[4,5]. Cardiovascular disease (CVD) is the most common comorbidity and the primary cause of mortality in CKD[6], with persistent low-grade inflammation recognized as a major but unaddressed driver of this pathology[7]. Although the gut microbiome strongly influences immunity[8], it is not yet targeted by standard CKD therapies. CKD is associated with an altered gut microbiome composition and production of metabolites entering the host circulation, including ligands of the aryl hydrocarbon receptor (AhR), a widely expressed transcription factor[9]. Indoxyl sulfate (IxS), a prototypical uremic toxin and agonistic AhR ligand, is derived from dietary tryptophan utilization by gut microbes and hepatic sulfation. Upon ligation and activation, the AhR translocates to the nucleus to regulate gene expression and immune cell differentiation[10]. AhR signaling contributes to inflammation[11], but its effects vary with ligand type, concentration, and context[12].

Here, we examine how gut microbiome-immune system interactions drive adverse cardiac remodeling in kidney disease. We show that microbiome depletion confers protection, while IL-17A emerges as a microbiome-dependent driver of cardiac fibrosis and dysfunction in CKD. IL-17A is increased in CKD patients and even more so with coexisting heart failure. Bacterial metabolite IxS promotes T_H17 differentiation via the AhR, and in heart failure, induces T_H17 and aggravates cardiac remodeling. Importantly, AhR inhibition suppresses T_H17 induction and cardiac fibrosis despite metabolite accumulation. Thus, we identify murine and human cardiac fibroblasts as AhR-modulated, IL-17A-responsive effectors. These findings reveal microbiome-dependent, pro-fibrotic pathways and position the AhR as a therapeutic target for cardiovascular protection in CKD.

Results

Gut microbiota accelerates cardiac remodeling in kidney disease

To assess the contribution of the gut microbiota to the host's response to kidney disease, we compared colonized and microbiome-depleted (oral antibiotics, Abx) 129/Sv mice subjected to subtotal nephrectomy (STNx), with sham-operated mice (Sham) as controls (Fig.1a). Disease progression was monitored over a 13-week period. Reduced 16S rRNA gene copies in cecal content confirmed successful microbiota depletion over the course of the experiment (Fig.S1a) and cecal weight was increased in Abx-treated mice, reminiscent of the germ-free (GF) mouse cecum (Fig.S1b)[13]. 16S rRNA gene sequencing of cecal samples from the non-microbiome-depleted groups showed a minor reduction in alpha diversity (Fig.S1c-e) in STNx mice while phyla composition remained similar (Fig.S1f). Principal component analysis (PCA) indicated a separation of bacterial communities (Fig.S1g). We found this to be due to an increase in known CKD-associated genera such as *Bacteroides* and *Ruminococcus* (Fig.S1h)[14]. Notably, the taxonomic shifts observed after STNx were less pronounced than those reported in patients with CKD[15], likely because factors such as diet and medication – major drivers of microbial variation in humans – are standardized or absent in our mouse model[16]. Functionally, bacterial metabolites are particularly relevant in kidney disease, as they can accumulate as a function of increased microbial production and insufficient renal excretion[5]. Thus, we performed plasma metabolomics by nuclear magnetic resonance (NMR), covering a large number of metabolites (Fig.1b). Antibiotic depletion led to a substantial reduction of metabolite accumulation in STNx mice, with most pronounced changes in the aromatic region of the NMR spectrum (Fig.1c). We therefore quantified a targeted panel of aromatic metabolites in plasma by mass spectrometry (MS, Fig.1d). Bacterially derived toxins such as indoxyl sulfate (IxS), p-cresol sulfate and phenyl sulfate were significantly increased in STNx (Fig.1e) and consequently reduced by Abx treatment. Thus, kidney disease induces taxonomic alterations in the microbiome and elevates bacterial metabolite concentrations in plasma, with both effects abrogated by microbiome depletion.

To assess the impact of microbiome depletion on the degree of kidney dysfunction, we measured glomerular filtration rate (GFR) longitudinally. While both STNx groups displayed a comparable initial GFR reduction until week 8 (Fig.1f), Abx-treated STNx

122 mice preserved higher GFR at the endpoint (Fig.1g) despite similar remnant kidney
123 mass (Fig.S2a). Measurement of plasma cystatin C (CysC), an endogenous filtration
124 marker, confirmed this observation (Fig.S2b).
125 Focusing on cardiovascular comorbidities as the leading cause of mortality in CKD[6,17],
126 we next assessed cardiac and vascular damage. STNx induced cardiac remodeling
127 as reflected by increased heart weight, which was abolished by microbiome depletion
128 (Fig.1h). Longitudinal echocardiographic assessment of cardiac dimensions
129 corroborated this effect, becoming evident from week 8 onward (Fig.1i-k; Table S1)
130 despite similar GFR at this time point. While systolic function (ejection fraction, EF)
131 was preserved in all groups (Fig. 1l; Table S1), STNx mice displayed an increase in
132 E/e' (Fig.1i, m; Table S1) indicative of diastolic dysfunction, and a reduction in global
133 longitudinal strain (GLS, Fig.1n; Table S1), reflecting ventricular stiffening – both
134 rescued by microbiome depletion. Adverse cardiac remodeling is characterized by
135 cardiomyocyte hypertrophy, fibrosis and inflammation[18]. Interestingly, we observed
136 comparable cardiomyocyte sizes in STNx (Fig.S2c-d), suggesting that the increased
137 heart weight is driven by extracellular matrix (ECM) deposition. Sirius Red staining
138 revealed increased collagen deposition in STNx hearts, which was mitigated in
139 microbiome-depleted STNx mice (Fig.1o-p). In addition, STNx mice exhibited
140 increased cardiac leukocyte infiltration (Fig.1q), comprising mostly neutrophils and T
141 cells (Fig.S2e), which was ameliorated in Abx-treated STNx mice. In agreement,
142 plasma C-reactive protein (CRP) – a routine clinical marker of systemic inflammation
143 associated with cardiovascular risk[19] – was elevated in STNx mice and reduced by
144 Abx treatment (Fig.1r). These findings demonstrate that microbiome depletion
145 prevents hallmarks of systemic inflammation, adverse cardiac remodeling and
146 diastolic dysfunction induced by kidney disease.
147 Reduced kidney function typically leads to hypertension, a common cause for adverse
148 cardiac remodeling. Further evidence suggests that the gut microbiota influences
149 blood pressure (BP) and cardiac remodeling[20,21]. We therefore measured BP
150 longitudinally by radiotelemetry in both control and Abx-treated STNx mice (Fig.1s).
151 Both groups exhibited a similar increase in both systolic BP (SBP) and diastolic BP
152 (DBP) throughout the experiment, which was sustained towards the study endpoint
153 (Fig.1t-u, S2f-i), suggesting that the cardioprotective effects observed in microbiota-
154 depleted STNx mice are independent of BP. To assess vascular function, we
155 measured vasorelaxation in isolated mesenteric arteries. Arteries from Abx-treated

156 STNx mice displayed an improved endothelium-dependent relaxation compared to
157 those from STNx mice (Fig.1v-w). Taken together, microbiome depletion protected
158 mice with reduced kidney function from further GFR loss, inflammation, cardiac and
159 vascular dysfunction despite a similar blood pressure increase, suggesting these
160 benefits are linked to immunological mechanisms.

161 **Microbiome-Dependent T_H17 Immunity and AhR Activation**

162 Since cardiac leukocyte influx was attenuated by microbiome depletion, we
163 hypothesized that microbiome-immune interactions are critical for the pathological
164 cardiac response to STNx. To assess immune cell composition, we performed flow
165 cytometry on splenic leukocytes (Fig.S3a). STNx induced an increased abundance of
166 neutrophils (Fig.2a) and a shift of T cells towards $CD4^+$ T helper subsets (Fig.2b), both
167 of which were prevented by Abx treatment. Flow cytometric analysis further revealed
168 an expansion of $CD44^+CD62L^-$ effector memory phenotypes (Fig.2c) for both $FoxP3^-$
169 conventional T helper cells (T_{conv}, Fig.2d) and $FoxP3^+$ regulatory T cells (T_{reg}, Fig.2e).
170 These alterations were abrogated in Abx-treated mice. Moreover, splenic T_{conv} from
171 STNx mice showed an increased abundance of RORγt$^+$ T_{conv} (T_H17, Fig.2f), which was
172 prevented by Abx. Similar patterns were detected in circulating and intestinal lamina
173 propria T cells (Fig.2g), indicating a microbiome-dependent T_H17-type inflammatory
174 response.

175 In parallel, we observed an expansion of RORγt$^+$ T_{reg}, hereafter referred to as $T_{reg}17$
176 cells (Fig.2h). While $T_{reg}17$ are known to limit inflammation in mucosal tissues[22], they
177 can also display T_H17-like effector functions, including IL-17A secretion[23]. To further
178 characterize $T_{reg}17$ in this inflammatory setting, we compared frequencies of PD-1$^+$,
179 CD69$^+$ and CD103$^+$ cells within the $T_{reg}17$ and T_{reg} compartment. $T_{reg}17$ cells showed
180 enrichment for these markers relative to total T_{reg} populations in Sham and Abx-treated
181 STNx mice; however, this pattern was not observed in STNx mice (Fig. S3b–d).
182 Additionally, IL-10$^+$ T_{reg} were reduced in STNx, but restored under Abx treatment
183 (Fig.S3e), altogether suggesting a loss of suppressive capacity favoring T_H17-like
184 effector functions. In line with these findings, STNx induced a sustained T_H17 and
185 $T_{reg}17$ increase over time (Fig.2i), while T_H17 of Sham and Abx did not show this
186 response. The parallel expansion of $T_{reg}17$ and T_H17 cells suggests ineffective
187 regulatory control and persistence of an inflammatory response.

188 Microbiota-derived metabolites can activate the aryl hydrocarbon receptor (AhR)[24],
189 which is known to modulate T cell function, including T_H17 differentiation[25,26].
190 Consistent with the observed increase in microbiome-derived tryptophan catabolites,
191 predominantly IxS, a known AhR ligand, plasma from STNx mice induced significantly
192 higher AhR activation in a cell-based reporter assay compared with Abx-treated and
193 Sham controls (Fig.2j). Moreover, *Cyp1a1*, a canonical AhR target gene, was
194 upregulated in splenic leukocytes from STNx mice compared to Abx-treated STNx
195 mice (Fig.2k), suggesting immune cells are affected by bacterial AhR ligands.

196 Next, we evaluated RORγt+ T cells in fibrotic hearts. We found an increase in $T_{reg}17$,
197 but not T_H17 cells, in whole hearts of STNx mice after 13 weeks (Fig.2l-m, Fig.S3f),
198 consistent with the observation that the cardiac microenvironment promotes T cell
199 transdifferentiation towards regulatory phenotypes[27]. Additionally, infiltrated
200 neutrophils were reduced in STNx mice treated with Abx (Fig.S3g). To further
201 characterize the inflammatory microenvironment of the heart, we performed bulk
202 mRNA sequencing from cardiac tissue. A substantial part of the STNx-associated
203 differentially expressed genes (DEG) were reversed by Abx treatment (Fig.2n).
204 Enrichment analysis on DEG identified Reactome pathways and Gene Ontology (GO)
205 terms involving tissue remodeling (e.g. fibronectin matrix formation, collagen
206 formation, extracellular matrix organization) and immunity (e.g. T cell receptor
207 signaling, interleukin 17 signaling, Fig.2o, S3h). Variation analysis of IL-17A-
208 associated gene sets revealed a significant increase in enrichment scores in STNx,
209 an effect normalized by Abx (Fig.2p). Taken together, our findings suggest that
210 microbiome-derived, AhR-activating metabolites drive a systemic T_H17-skewed
211 inflammatory response that impairs $T_{reg}17$ function and promotes adverse cardiac
212 remodeling in kidney disease.

213 **IxS exacerbates heart failure**

214 IxS has been shown to modulate T_H17 immunity in neuroinflammation[28]. *In vitro* T_H17
215 polarization of murine naïve CD4+ T cells was indeed stimulated dose-dependently by
216 IxS (Fig.3a-b). To test whether IxS stimulates a T_H17 response *in vivo* and aggravates
217 cardiac remodeling independent of advanced kidney dysfunction, we examined the
218 effects of IxS supplementation in a mouse model of heart failure with preserved
219 ejection fraction[29] (HFpEF, Fig.3c), the form of heart failure most frequently associated
220 with CKD[30]. We confirmed elevated IxS levels in mice exposed to IxS (Fig.3d),

221 although to a lesser extent compared to STNx mice and patients with CKD[31], likely
222 due to preserved renal clearance (Fig.3e). Still, IxS levels were sufficient to increase
223 splenic *Cyp1a1* expression (Fig.3f), but not liver *Cyp1a1* (Fig.S4a), indicating that the
224 immune system is particularly susceptible to AhR activation by bacterial metabolites.
225 Similar to STNx mice, splenic IL-17A$^+$ T_{conv} (Fig.3g), IL-17A$^+$ T_{reg} (Fig.3h) and
226 neutrophils (Fig.S4b) frequencies were elevated in response to IxS. IxS exposure
227 exacerbated heart failure, evidenced by increased heart weights (Fig.3i) and
228 pulmonary congestion (Fig.S4c). Echocardiography confirmed aggravation of diastolic
229 dysfunction (E/e', E/A, Fig.S4d-e; Table S2) with a preserved left ventricular EF
230 (Fig.S4f; Table S2). Next, we analyzed cardiac fibrosis, the most prominent feature of
231 STNx-associated cardiac remodeling. IxS-exposed hearts displayed higher collagen I
232 and fibronectin content, indicating increased interstitial cardiac fibrosis (Fig.3j-l). Thus,
233 IxS exacerbates heart failure and fibrosis, and elicits a similar inflammatory response
234 as observed in experimental kidney disease.

235 **Cardiac fibroblasts respond to IL-17A and IxS to produce ECM**

236 In addition to the T cell-driven increase in IL-17A production, *Il17ra* expression was
237 upregulated in STNx hearts (Fig.4a), and likewise in IxS-treated HFpEF mice (Fig.4b).
238 To identify IL-17A-responsive cells among cardiac cells, we re-analyzed published
239 single nuclei RNA (sn-RNA) sequencing data from cardiac tissue of STNx and control
240 mice[32]. Among cardiac cell types, fibroblasts showed the highest *Il17ra* expression in
241 STNx (Fig.4c, Fig.S5a). Notably, fibroblasts also showed higher expression of AhR-
242 dependent genes (Fig.S5b) Interestingly, *Il17ra*$^+$ fibroblasts displayed higher ECM
243 gene set scores[33] than *Il17ra*$^-$ fibroblasts in STNx mice (Fig.4d). In line, the DEG were
244 characterized by a dominant representation of ECM components (Fig.S5c). To further
245 characterize *Il17ra*$^+$ fibroblast transcriptomes, we compared their DEG with different
246 fibroblast signatures known in both mouse and human cardiac tissue[34]. DEG were
247 enriched in myofibroblast-related and, to a lesser degree, cyclic and WNT-related
248 fibroblast-specific genes (Fig.4e), known for their pro-fibrotic and activated status.
249 Cytokine enrichment analysis revealed IL-17A as a prominent factor shaping DEG in
250 cardiac STNx lymphocytes (Fig.S5d). To test the response of cardiac fibroblasts to
251 AhR ligand IxS and IL-17A, respectively, we isolated fibroblasts from healthy murine
252 hearts (Fig.4f). Cell identity and purity were confirmed by immunocytochemistry and
253 flow cytometry (Fig.4g-h). As suggested by the sn-RNA data, IxS upregulated *Il17ra*

254 mRNA expression (Fig.4i), indicating IxS primes fibroblasts to sense IL-17A.
255 Consistent with this, coincubation with IL-17A and IxS resulted in a synergistic
256 increase in *Col1a1*, *Col1a2*, and *Acta2* expression (Fig.4j-l). In line with *in vivo* data,
257 IL17A downregulated *Abi3bp* expression, an ECM protein shown to be reduced in
258 heart failure[35] (Fig.4m). Immunocytochemistry confirmed the presence of COL1 and
259 IL17RA at the protein level (Fig.4n). Our data demonstrate that IL-17A signaling in
260 cardiac fibroblasts primed by IxS exposure leads to increased ECM production,
261 ultimately exacerbating cardiac fibrosis.

262 **AhR inhibition ameliorates cardiac remodeling in kidney disease**

263 Since STNx-associated cardiac remodeling occurs in an AhR-activating milieu that in
264 turn promotes IL-17A production and cardiac fibrosis, we investigated whether AhR
265 inhibition confers therapeutic benefit. For optimal translational potential, we re-
266 purposed the orally bioavailable AhR inhibitor BAY 2416964 (AhRi), currently under
267 investigation in solid malignancies[36]. *In vitro*, AhRi dose-dependently reduced the IxS-
268 induced upregulation of *Cyp1a1* expression in murine splenocytes (Fig.5a-b).
269 Furthermore, AhRi dose-dependently suppressed IxS-driven T_H17 polarization
270 (Fig.5a,c). In both assays, AhRi was effective at doses of $10^{-7.5}$-$10^{-6.5}$ M. Next, we
271 aimed to test the efficacy of AhRi *in vivo* in STNx mice (Fig.5d). Therefore, mice were
272 stratified according to their CysC levels (Fig.S6a) and randomized to receive either
273 AhRi or vehicle starting two weeks after complete STNx through to week 13 by daily
274 oral gavage. Sham-operated vehicle-treated mice served as additional control. At the
275 endpoint, we detected similar levels of CysC in AhRi- and vehicle-treated mice
276 (Fig.S6b). AhRi treatment improved survival of STNx mice (Fig.5e) and lowered
277 systemic inflammation, as measured by plasma CRP (Fig.5f). Upregulation of
278 canonical AhR target gene *Cyp1a1* in immune cells was prevented by AhRi (Fig.5g),
279 as well as the STNx-associated increase in both T_H17 (Fig.5h) and $T_{reg}17$(Fig.5i). In
280 line, IL-17A+ T_{conv} and T_{reg} were reduced by AhRi (Fig.S6c-d). We observed an
281 improvement of the cardiac phenotype upon AhRi reminiscent of the Abx effect, with
282 lower left ventricular mass (Fig.5j), and improved cardiac function (Fig.5k-l, Table S3)
283 and reduced fibrosis (Fig.5m-n), together with lower cardiac *Il17ra* expression (Fig.5o).
284 Bulk transcriptomic analyzes of cardiac tissue showed similar effects as observed with
285 Abx treatment, with a reduction in GO terms and pathways involved in ECM formation
286 and inflammatory processes (Fig.5p, Fig.S6e). Targeted analysis of T_H17-related

287 signaling pathways revealed significantly higher scores upon STNx, which were
288 rescued by AhRi (Fig.5q). These findings identify the AhR as a key mediator of
289 inflammation and cardiac remodeling in kidney disease and suggest AhRi as a
290 therapeutic strategy.

291 **Conserved pro-fibrotic IxS-AhR-T_H17 axis in patients with CKD**

292 We further aimed to explore the translational potential of AhRi by investigating the
293 efficacy in human cells. AhRi dose-dependently blocked the IxS-stimulated AhR
294 activity in human AhR reporter cells (Fig.6a). Likewise, AhRi reduced the AhR
295 activating potential of serum collected from patients with kidney failure requiring
296 hemodialysis (HD) to levels observed with serum from healthy controls (HC, Fig.6b-c;
297 Table S4). Moreover, addition of HD serum to human T_H17 polarization assays
298 increased T_H17 cells compared to HC (Fig.6b,d). Hence, the kidney disease-
299 responsive AhR-T_H17 axis identified in mice appears to be conserved in humans.
300 Next, we analyzed plasma IL-17A levels in patients with CKD and HC from the UK
301 Biobank (Table S5). Circulating IL-17A concentrations increased progressively with
302 decreasing eGFR and increasing albuminuria, the two main determinants of CKD
303 (Fig.6e, n = 15 120 with available eGFR and albuminuria). IL-17A concentrations were
304 further elevated in patients with eGFR below 60 ml/min/1.73 m^2 (CKD) and HFpEF
305 (n = 5 497) compared to patients with eGFR below 60 ml/min/1.73 without HFpEF
306 (n = 15 981, Fig.6f). Furthermore, higher plasma IL-17A in individuals with CKD
307 (n = 2 785) was associated with all-cause mortality, even after adjustment for
308 conventional risk factors (Fig.6g-h). These findings substantiate kidney disease-
309 dependent IL-17A response at population scale.
310 To verify the role of AhR signaling and IL-17A in fibroblast activation in humans, we
311 used publicly available single cell RNA (sc-RNA) sequencing data. Since cardiac sc-
312 RNA data from patients with CKD were not available, we explored data from kidney
313 tissue of patients with CKD and healthy controls[37]. Fibroblasts of patients with CKD
314 displayed the highest AhR enrichment scores compared to other kidney cell types
315 (Fig.S7a). Moreover, myofibroblasts expressed the highest levels of *IL17RA* (Fig.S7b),
316 and *IL17RA* expressing myofibroblasts exhibited markedly higher ECM module scores
317 (Fig.S7c). In line, pro-fibrotic and ECM-associated genes were among the major DEG
318 (Fig.S7d), indicating that IL-17A-responsive fibroblasts represent a pro-fibrotic subset.

319 Next, we stimulated primary human cardiac fibroblasts with serum from hemodialysis
320 patients (HD) or healthy controls (HC) (Fig.6i). HD serum induced upregulation of
321 *IL17RA* (Fig.6j, Fig.S8a) together with ECM-associated transcripts such as *COL1A2*
322 and *ACTA2* (Fig.6k-m, Fig.S8b-d). We tested whether these effects could be
323 prevented by AhRi or secukinumab, a human monoclonal antibody used in clinical
324 routine targeting IL-17A (αIL-17A). Both AhRi and αIL-17A mitigated the pro-fibrotic
325 effects (Fig.6k-m, Fig.S8b-d). However, only AhRi reduced *IL-17RA* expression
326 (Fig.6j, Fig.S8a). Similar to murine cardiac fibroblasts, IxS upregulated *IL17RA*
327 expression in primary human cardiac fibroblasts, an effect abrogated by AhRi
328 (Fig.S8e). Both IxS and IL-17A increased *COL1A2* and *ACTA2* expression, whereas
329 co-stimulation with both ligands again had a synergistic effect, leading to the highest
330 pro-fibrotic transcriptional response (Fig.S8f-h). Proliferation was not altered with IL-
331 17A and IxS co-incubation, as determined by Ki-67 staining (Fig.S8i-j). Taken
332 together, interrogating data from UK Biobank, human sc-RNA sequencing and *in vitro*
333 assays using patient-derived serum show a conserved pro-fibrotic IxS-AhR-T_H17 axis
334 in CKD.

335 **Discussion**

336 This study demonstrates that kidney disease recalibrates microbiome-host
337 interactions to potentiate inflammation-mediated cardiac fibrosis. We identify a
338 microbial AhR-activating metabolite driving a pathogenic T_H17 response that engages
339 IL-17A-responsive cardiac fibroblasts, positioning the metabolite-AhR-IL-17A axis as
340 a therapeutic target to prevent cardiac fibrosis in kidney disease.
341 Inflammation is a key driver of CVD. In CKD, inflammation is substantially elevated,
342 paralleling a markedly increased risk for CVD[38]. Evidence suggests that CVD
343 development in CKD extends beyond traditional risk factors[39] such as hypertension,
344 hyperlipidemia, and diabetes, yet underlying mechanisms remain less characterized.
345 Adverse cardiac remodeling and fibrosis are prevalent in CKD[40], with heart failure
346 representing a frequent clinical manifestation[41]. The microbiome plays a central role
347 in immune modulation, in part via action of bacterial metabolites. In CKD, these
348 metabolites accumulate and contribute to a pro-inflammatory internal milieu. Such
349 metabolites were shown to be of bacterial colonic origin and can reach toxic levels in
350 CKD[5]. To date, therapeutic strategies aimed at improving outcomes by reducing
351 bacterial metabolite levels through unspecific intestinal adsorption showed limited
352 success[42], underscoring the need for a refined understanding of microbiome-host
353 interaction in CKD.
354 Our mechanistic investigations were prompted by the observation that the depletion
355 of the gut microbiome in a state of reduced kidney function drastically reduced the
356 development of cardiac fibrosis as well as diastolic dysfunction, and suppressed
357 systemic inflammation, as evidenced by a lower plasma CRP. Remarkably,
358 cardioprotection occurred despite persistently high blood pressure, in line with a
359 clinical observation showing that cardiac fibrosis in CKD occurs independent of
360 hypertension[40], which has so far not been linked to the gut microbiome. The profound
361 inflammation encouraged us to investigate cellular immunity further, in which a
362 microbiome-dependent T_H17 response to STNx became evident. While IL-17A has
363 previously been associated to ischemic heart disease[43] and kidney disease
364 progression after acute kidney injury[44], it has not been highlighted as a cytokine linking
365 heart disease and CKD. Our analyzes of UK Biobank data corroborate this link,
366 demonstrating elevated IL-17A levels in patients with CKD and HFpEF. IL-17A plasma

concentrations increased with increasing severity of CKD, reflected by decreasing eGFR or increasing albuminuria and were associated with excess mortality.

We previously hypothesized that CKD-linked inflammation is mediated by the AhR[26]. Plasma AhR activation potential and AhR-dependent gene expression in splenocytes increased following STNx; both effects being abrogated by microbiome depletion. We also present evidence that AhR activation and T_H17 response are mediated via the AhR by increased levels of IxS, a known microbiome-derived AhR-activating ligand. *In vitro*, IxS induced T_H17 polarization dose-dependently. *In vivo*, oral administration of IxS in an experimental heart failure model increased AhR activation and AhR-dependent gene expression in immune cells, promoted T_H17 expansion, and aggravated cardiac fibrosis, despite preserved kidney function. Further *in vivo* evidence is provided by AhR inhibition in STNx mice, which abrogated AhR-dependent gene expression in immune cells, T_H17 expansion and systemic inflammation, as well as cardiac fibrosis and diastolic dysfunction. Thus, IxS-dependent AhR activation appears to be central to cardiac remodeling in kidney disease.

As an environmental sensor integrating various external and endogenous cues, the AhR is known to regulate T_H17 differentiation[45]. AhR-deficient naïve T cells exhibit reduced differentiation[45], while AhR activation by high affinity ligands has been shown to promote T_H17 and autoimmune disease[46]. However, AhR-mediated effects on T_H17 differentiation depend on the ligand and cytokine milieu[47]. IxS is a known endogenous AhR ligand[28] and has been linked with inflammatory milieus[48] as well as T_H17-mediated autoimmunity[28]. We present evidence that IxS activates AhR transcriptional programs in CD4+ cells to promote a pathogenic T_H17 response in kidney disease. We show that IxS drives RORγt expression and IL-17A production in CD4+ T cells *in vitro* and *in vivo*. Intriguingly, we also detected increased IL-17A production by Foxp3+ CD4+ T_{reg}, as well as increased RORγt expression in CD4+ FoxP3+ cells ($T_{reg}17$), especially in cardiac tissue. While $T_{reg}17$ cells typically restrain IL-17A-driven inflammation through IL-10[48], their regulatory capacity appears diminished in the present uremic setting, where IL-17A-mediated inflammation is less effectively controlled. Consistently, $T_{reg}17$ cells from uremic STNx mice exhibited reduced expression of PD-1, CD103, and CD69 – proteins implicated in the maintenance of suppressive function[49-51] – compared to microbiome-depleted mice with kidney failure and healthy control mice. This phenotype suggests a functional shift in $T_{reg}17$ cells toward RORγt-driven effector activity at the expense of FoxP3-dependent regulatory

401 functions. Moreover, IL-10 production was lowest in T_{reg}s from STNx mice. The STNx-
402 induced IL-17A response was accompanied by neutrophilia and enhanced cardiac
403 neutrophil infiltration. IL-17A is a known regulator of neutrophils, promoting
404 granulopoiesis and inducing neutrophil-attracting chemokines in stromal and cardiac
405 cells[52]. Circulating neutrophils correlate with IL-17A levels[53]. Once recruited,
406 neutrophils maintain IL-17A-driven inflammation through release of inflammatory
407 mediators, including IL-1β and neutrophil extracellular traps[54]. Together, these
408 findings reveal a microbiome-dependent, AhR-mediated and IL-17A-driven
409 inflammatory program in kidney disease.
410 Our study identifies cardiac fibroblasts as key targets of IL-17A, characterized by
411 enhanced IL-17RA expression *in vivo*, which in turn drives ECM production and
412 promotes cardiac fibrosis. It has previously been reported that IL-17A enhances
413 fibroblast proliferation and migration[55] and induces a proinflammatory fibroblast
414 phenotype involving GM-CSF[56]. We demonstrate that IxS effectively primes cardiac
415 fibroblasts via AhR-dependent upregulation of IL-17RA in murine and human cells,
416 suggesting that the same bacterial metabolite that drives IL-17A-mediated
417 inflammation also sensitizes fibroblasts to IL-17A signaling and ECM production. Thus,
418 IxS orchestrates inflammation and tissue remodeling through AhR signaling, providing
419 a mechanistic explanation for the pronounced cardiac fibrosis observed in CKD and a
420 strong rationale for AhR inhibition as a therapeutic strategy. Notably, pharmacological
421 AhR targeting with a small-molecule inhibitor currently under clinical investigation for
422 cancer treatment[36] (NCT04999202) proved effective both *in vivo* in STNx mice and *in*
423 *vitro* in human cardiac fibroblasts, highlighting its translational potential. Targeting host
424 sensing of uremic toxins may uncouple disease-driving microbiome-derived
425 metabolites from downstream inflammatory responses. Integrating AhR inhibition with
426 existing therapies could therefore provide a complementary strategy to mitigate
427 adverse cardiovascular comorbidities in CKD.
428 Taken together, our findings identify an IxS-AhR-IL-17A axis as a central driver of
429 cardiac inflammation and fibrosis in kidney disease. We thereby demonstrate how
430 kidney dysfunction promotes cardiac pathology through specific microbiome-derived
431 metabolites. Our study positions IxS not merely as a biomarker of uremia but as an
432 active pathogenic effector linking microbial metabolite accumulation to maladaptive
433 immunity and tissue fibrosis via AhR signaling. AhR inhibition may offer a means to
434 selectively target uremic downstream signaling while preserving potentially beneficial

microbiome functions. More broadly, these findings refine our knowledge of disease-to-multimorbidity transition, moving beyond traditional organ-centered models toward a mechanistic understanding of inter-organ communication and highlighting the microbiome as an upstream driver of host response reprogramming that facilitates pathological organ crosstalk.

Methods

Animal studies

All experiments were performed in accordance with the German/European law for animal protection. Experimental protocols were approved by the local ethic authorities under the G0190/21 and G0019/21 licenses. For all *in vivo* experiments, male 129/Sv mice (wild type [WT]; strain 129S2/SvPasOrlRj) were obtained from Janvier Labs, France, and housed at 12-hour day:night cycle with free access to water and food (Chow diet, Ssniff, V1124-300) in the Preclinical Research Center (PRC) of the Max-Delbrück-Center for Molecular Medicine (MDC). Mice were habituated for 2 weeks before use. Individual mice served as experimental units, and all animals within a cage received the same treatment.

For the Abx trial, mice were distributed according to body weight (BW) to four groups prior to treatment (STNx ± Abx and Sham ± Abx). The Abx experiment consisted of two independent cohorts. A longitudinal cohort was designed to evaluate dynamics in kidney function, metabolomics and immunity in STNx groups (n=11 per group) and Shams (n=7 per group) across timepoints (w1, w3, w8, w13). Each timepoint had its own independent cohort to collect biomaterial. A second cohort was designed for terminal assessments, focused on organ damage and tissue level responses in STNx groups (n=12) and Shams (n=7). Both cohorts were exploratory, thereby no prior sample size calculation was performed. Endpoint analyzes were performed combining both cohorts if applicable. Animals were excluded in cases of surgical failure or failure to reach minimum kidney function thresholds. Animals were sacrificed during the course of the study if BW dropped under 20% or they showed clear signs of pain or discomfort. The longitudinal cohort resulted in: w1 - Sham n=7; Abx n=6; STNx n= 6; STNx Abx n= 6. w3 - Sham n=6; Abx n= 7; STNx n=10; STNx Abx n=7. w8 - Sham n=5; Abx n=5; STNx n=6; STNx Abx n=6. w13 - Sham n=6; Abx n=4; STNx n=6; STNx Abx n=6. The endpoint cohort resulted in: Sham n=7; Abx n=7; STNx n=11; STNx Abx n=10.

For the HFD/L-NAME trial, mice were assigned according to BW and cage to receive either potassium indoxyl sulfate (IxS) exposure (n=16) or control (KCl; n=16) over the drinking water *ad libitum.* Sample size was calculated using G Power according to a partial effect size of the alleviation of the STNx-induced diastolic dysfunction by Abx.

472 During the experiments n=3 from the control group were taken out of the experiment
473 due to prespecified criteria.

474 For the AhRi trial, mice underwent STNx (n=24) or Sham (n=6) surgery. Sample size
475 was calculated using G Power according to the effect size of the alleviation of the
476 STNx-induced cardiac fibrosis by Abx. The same exclusion criteria were followed as
477 in the Abx trial. To ensure equal kidney dysfunction before treatment, mice were
478 equally distributed into 2 groups according to BW and plasma CysC two weeks after
479 completed STNx surgery, and assigned to receive either AhRi (n=10) or vehicle (n=9).
480 During the experiments n=4 vehicle and n=2 AhRi-treated animals were taken out of
481 the experiment due to prespecified criteria and analyzed at an earlier time point.

482 Across all experiments, blinding during *in vivo* procedures was not possible due to
483 model-specific features; however, all outcome measurements and data analysis were
484 performed blindly.

485 Subtotal nephrectomy

486 Mice between 10 and 12 weeks old were anaesthetized with isoflurane (2.5%
487 isoflurane-air) and subjected to subtotal nephrectomy operation (STNx). Briefly, the
488 left kidney was exposed, and the lower and upper poles were excised using a
489 cauterizer (Surtron 160, LED SpA). The adrenal gland was separated from the kidney
490 to preserve its function. 2 weeks later, a total nephrectomy of the right kidney was
491 performed. Sham-operated mice underwent a simple flank incision and sutures. All
492 animals received pre-emptive buprenorphine (30 mg/kg, intraperitoneal (i.p.) injection)
493 30 min before surgery. Post surgery, analgesia consisted of metamizole (800
494 mg/kg/24h) administered over the drinking water for 3 days.

495 Antibiotic treatment

496 Mice were given an antibiotic cocktail (all obtained individually from Thermofisher)
497 containing ampicillin (0.5 g/L), vancomycin hydrochloride (0.5 g/L), neomycin sulfate
498 (1 g/L) and metronidazole (1 g/L) in the drinking water throughout the entire study
499 period. 1% glucose was added into the mixture for organoleptic purposes. Control
500 animals received only glucose in the drinking water. Treatment was started one week
501 prior to the first operation and antibiotics were refreshed every 3 days.

502 AhR inhibitor treatment

503 Mice were stratified and randomized as described above to receive either small-
504 molecule AhR inhibitor BAY2416964 (GlpBio) or vehicle, starting two weeks after
505 completed STNx surgery. AhRi was formulated in a mixture of water, Solutol® HS 15
506 (polyethylene glycol 12-hydroxystearate; Merck) and ethanol at a 50:40:10 ratio
507 (v/v)[36]. The vehicle control consisted of the solvent mixture alone. A daily AhRi dose
508 of 30 mg/kg was selected based on a previously reported safe and effective regimen[36].

509 HFpEF model

510 12-week-old mice were switched to a high fat diet (HFD; 60% kcal fat, Research diets,
511 D19032801-1.5V) and administered Nω-nitro-L-arginine methyl ester hydrochloride
512 (L-NAME; 1 g/L, Merck) in the drinking water for 15 weeks. Mice received either
513 potassium indoxyl sulfate (IxS; 1 g/L, Merck) or equimolar potassium chloride (KCl;
514 0.3 g/L, Merck) in the drinking water throughout the study. This model has been
515 published previously[29].

516

517 **Microbiome**

518 Cecal DNA isolation

519 At different timepoints (w1, w3, w8, w13), cecal contents were collected at the time of
520 euthanasia. Samples were immediately fresh-frozen on dry ice and kept at -80 °C.
521 DNA was isolated from cecal samples using the Quick-DNA Miniprep Kit (Zymo
522 Research) according to manufacturer's protocol. Absolute bacterial load was
523 determined by qPCR for the *16S* gene using SYBR Green as described below.

524 Microbiome analysis

525 Samples were stored at -20°C and sent for 16S rRNA gene amplicon sequencing
526 (Novogene, Cambridge, UK). The V3-V4 hypervariable region of the 16S rRNA gene
527 was amplified using universal primers 341F (5′-CCTAYGGGRBGCASCAG-3′) and
528 806R (5′-GGACTACNNGGGTATCTAAT-3′), which were appended with sample-
529 specific barcodes and Illumina sequencing adapters. Amplicons were purified using
530 AMPure XP magnetic beads and quantified for library preparation.

531 Libraries were constructed using the NEBNext® Ultra™ II DNA Library Prep Kit and
532 sequenced on an Illumina NovaSeq 6000 platform (paired-end 2×250 bp), targeting

533 approximately 30,000 raw reads per sample. Annotation was performed in R (v4.0.3).
534 Demultiplexed reads were processed through DADA2 pipeline (v1.25.2) and
535 taxonomic assignment was based on the rRNA database SILVA (v138.1) with a 80%
536 boodstrapped confidence. Only ASVs that were present in at least 20% of the samples
537 were considered for further downstream analysis.

538

539 **Nuclear magnetic resonance (NMR) spectroscopy**

540 Sample preparation

541 Plasma samples were prepared using 3 mm SampleJet NMR tubes. 100 µL of plasma
542 was mixed thoroughly with 78 µL of 0.1 mol/L phosphate buffer (pH 7.4) and 19.5 µL
543 of a 0.75% (w) solution of 3-trimethylsilyl-2,2,3,3-tetradeuteropropionate (TSP; Sigma-
544 Aldrich, Taufkirchen, Germany) in deuterium oxide, serving as an internal standard for
545 NMR measurements. As an additional internal standard 2.5 µL of formic acid (240
546 mM) was added. Prepared samples were measured as described below.

547 Data acquisition

548 All NMR experiments were performed on a 600 MHz Bruker Avance III HD
549 spectrometer, using a triple resonance (^{1}H, ^{13}C, ^{15}N, ^{2}H lock) helium cooled cryoprobe
550 with z-gradient. Samples were handled by an automatic Bruker SampleJet sample
551 changer (Bruker Biospin GmbH, Ettlingen, Germany). Tuning and matching of the
552 probe as well as locking and shimming of the sample were performed automatically.
553 For each sample one dimensional ^{1}H NMR spectra were obtained at 310 K using Carr-
554 Purcell-Meiboom-Gill (CPMG) pulse sequence. For each spectrum, 512 scans were
555 collected into 72k datapoints over a spectral width of 12019 Hz. An acquisition time
556 and T_1 relaxation delay of 3.07 and 4 seconds per scan were used, respectively. All
557 NMR spectra were processed with TopSpin 4.5.0. Free induction decays (FIDs) were
558 Fourier transformed, phase corrected and subjected to exponential line broadening
559 function of 0.3 Hz. All the chemical shifts were manually referenced to formic acid at
560 8.46 ppm.

561 To compensate for chemical shifts perturbations bucket tables were generated from
562 the processed 1D CPMG spectra using AMIX software (version 3.9.13, Bruker,
563 Ettlingen, Germany). The spectra over a range from δ0.11 to δ 9.5 ppm were divided

564 into the buckets at an equal width of 0.01 ppm with the regions at δ4.59 - δ4.77 ppm
565 being excluded as the water peak. The spectra were not normalized.

566 Bucket analysis

567 Only buckets within the aromatic region (6.75-8.00 ppm) were retained for subsequent
568 analyzes. For each treatment background, sham animals were used to calculate the
569 mean intensity for every aromatic bucket, providing treatment-matched reference
570 values. Each STNx (± Abx) sample was then compared with its corresponding sham
571 reference by determining, for each bucket, whether its intensity exceeded the sham
572 mean. The proportion and number of aromatic buckets classified as increased were
573 calculated per sample and statistically compared between groups using Mann Whitney
574 U test.

575

576 **Liquid chromatography-mass spectrometry**

577 Tryptophan panel

578 Tryptophan and its downstream metabolites were quantified in serum and plasma
579 samples. If not stated otherwise, the sample preparation was applied as stated
580 previously[57]. Briefly, 10 µL of an aqueous stable-isotope labelled internal standard
581 mixture was added to 50 µL of serum/ plasma. For protein precipitation samples were
582 diluted in a ratio of 1:5 with 100% cold methanol, vortexed, and stored at -80 °C for
583 24 h. Samples were centrifugated at 10,000×g at 4 °C for 5 min. The supernatant was
584 collected. The protein pellet was washed twice by addition of 200 µL of cold 80%
585 MeOH and subsequent centrifugation at 10,000×g (washing step 1) and 12,000×g
586 (washing step 2) at 4 °C for 5 min. For each sample, all supernatants were combined
587 and dried using a vacuum evaporator (CombiDancer, Hettich AG, Bäch, Switzerland).
588 All samples were reconstituted in 100 µL in water.

589 An ExionLC-30AD HPLC system (AB Sciex, Germany, Darmstadt) was used for the
590 chromatographic separation of metabolites on an ACQUITY Premier HSS T3, 1.8 µm,
591 2.1 × 150 mm reversed-phase column (Waters, Eschborn, Germany) reversed-phase
592 column. Gradient elution was performed with mobile phase A consisting of 0.1% formic
593 acid in water and mobile phase B of 0.1% formic acid in acetonitrile. Metabolite
594 detection was performed with a TripleQuad6500^{+} (AB Sciex, Germany, Darmstadt)
595 performing positive/ negative-switching for the ionization. Peak integration and data

596 evaluation were carried out using SciexOS-MQ Software (Version 2.1.6, AB Sciex,
597 Germany, Darmstadt). Results were normalized to sample volumes.

598 3-Indoxyl sulfate quantification

599 For the HFD/L-NAME trial, frozen plasma samples were thawed at RT and then 70 µL
600 of each sample was mixed with 210 µL of a cold methanolic solution of the internal
601 standard d_5-IxS (Toronto Research Chemicals, Toronto, Canada), concentrated to
602 1 µmol/L . Proteins were precipitated by vortexing for 1 min and subsequent storage
603 for 60 min at -20°C. Supernatants were obtained by centrifugation at 9,400 g at 4°C
604 for 10 min and subjected to LC-MS/MS IxS quantification applying the multiple reaction
605 monitoring (MRM) method. Chromatographic separation was achieved on a 1290
606 Infinity II HPLC (Agilent Technologies, Waldbronn, Germany) equipped with a
607 Poroshell 120 EC-C18 column (3.0 x 150 mm, 2.7 µm; Agilent Technologies) guarded
608 by a pre-column (3.0 x 5 mm, 2.7 µm) of identical material. Water (eluent A) and
609 acetonitrile (eluent B), both acidified with 0.1% formic acid, were pumped with
610 0.4 mL/min. Elution of IxS and its internal standard was achieved with a 10-min linear
611 gradient from 5% to 90% eluent B. Total run-time was 16 min including re-equilibration
612 of the LC system. MS/MS analyzes were carried out using an Ultivo (6465B) triple-
613 quadrupole mass spectrometer (Agilent Technologies) operating in the negative
614 electrospray ionization mode (ESI-). The following ion source parameters were set:
615 sheath gas temperature, 400°C; sheath gas flow, 12 l/min of nitrogen; nebulizer
616 pressure, 50 psi; drying gas temperature, 100°C; drying gas flow, 9 l/min of nitrogen;
617 capillary voltage, 2.0 kV; nozzle voltage, 0.4 kV. The following mass transitions were
618 recorded (fragmentor voltage [FV] and collision energies [CE] in parentheses): IxS:
619 *m/z* 212.0 → 79.8 (FV: 102 V, CE: 28 eV, quantifier), *m/z* 212.0 → 80.9 (FV: 102 V,
620 CE: 16 eV), *m/z* 212.0 → 131.9 (FV: 102 V, CE: 20 eV), d_5-IxS: *m/z* 217.0 → 79.8 (FV:
621 82 V, CE: 28 eV, quantifier), *m/z* 217.0 → 80.9 (FV: 82 V, CE: 16 eV), *m/z* 217.0 →
622 137.0 (FV: 82 V, CE: 20 eV). Peak areas were determined with MassHunter
623 Quantitative Analysis software (version 10.1, Agilent Technologies) and IxS was
624 directly quantified via its internal standard d_5-IxS that was concentrated to 750 nmol/L
625 in the samples.

626 **Transdermal measurement of glomerular filtration rate**

627 FITC-sinistrin was reconstituted with PBS (40 mg/mL) and stored at -20 °C. Mice were
628 anaesthetized with isoflurane and prone-placed on a heat pad. After shaving, the GFR
629 monitor was attached on the right side of the back below the ribs. The measurement
630 was recorded for 2-3 minutes prior to intravenous FITC-sinistrin injection (60 mg/kg)
631 via either the tail vein or retro-orbital injection to set a steady baseline. Mice were then
632 allowed to recover from anesthesia for the measurement of FITC decay (1-2 hours).
633 Transcutaneous GFR was calculated from FITC-sinistrin half-time using a 3-
634 compartment model (MBLab2, Medibeacon).

635

636 **Clinical chemistry**

637 Clinical parameters (plasma CRP, Cystatin C) were analyzed using an AU480 clinical
638 chemistry analyzer (Beckman Coulter).

639

640 **Echocardiography**

641 Echocardiography was performed according to a standard operation protocol[58].
642 Briefly, mice were examined on a Vevo 3100 Imaging System equipped with a 30 MHz
643 linear transducer (MX400; FUJIFILM VisualSonics Inc., Canada). Anaesthesia was
644 induced by 3% isoflurane (in 80% oxygen). For image acquisition, isoflurane
645 concentration was reduced to 1-1.5%, and adjusted to maintain comparable heart
646 rates. All images were analyzed using Vevo LAB analysis software (FUJIFILM
647 VisualSonics Inc.). Systolic function and cardiac dimensions were assessed using B-
648 mode and M-mode echocardiography obtained from the parasternal long-axis view
649 and the parasternal short-axis view at the mid-papillary level. Diastolic function was
650 evaluated using conventional pulsed-wave Doppler to measure transmitral flow in the
651 apical four-chamber view. Tissue Doppler recordings from the septal mitral annulus
652 were used to assess myocardial relaxation velocity. The following parameters were
653 analyzed: E/A (early diastolic filling velocity to atrial contraction), E/e′ (early filling
654 velocity to early diastolic annular motion), and IVRT (isovolumetric relaxation time).
655 Strain and M-mode measurements were derived from three images per parameter,
656 with three cardiac cycles per image, and subsequently averaged. Diastolic Doppler
657 measurements were obtained from three independent images, each with three

658 repeated measurements. Speckle-tracking analysis was performed using parasternal
659 long-axis and short-axis images, with epicardial and endocardial contours used to
660 quantify longitudinal, circumferential, and radial deformation[59]. Echocardiographic
661 parameters for each trial are summarized in Tables S1–S3.

662

663 **Cardiac histology**

664 Hearts were immediately collected after sacrifice. Cardiac tips were snap-frozen at
665 -80 °C for RNA isolation. The remaining tissue was either fixed in 10% neutral buffered
666 formalin solution (Merck) for 36 h at room temperature (RT) and then switched to 1%
667 until further use, or fixed in 4% paraformaldehyde (PFA) in PBS for 5 h at 4 °C.

668 For Picrosirius Red staining (PSR), formalin-fixed heart tissues were embedded in
669 paraffin and transversally sectioned (2 µm) using an HM 340E Rotary Microtome
670 (Epredia). Prior to staining with PSR, tissue sections were deparaffinated, rehydrated,
671 washed and incubated in PSR working solution (Morphisto) according to
672 manufacturer's protocol, with the exception of using ROTIClear (Carl Roth) as a xylol
673 substitute. After washing and dehydration, samples were mounted in water-free
674 medium (ROTIMount, Carl Roth, HP68.1).

675 For IHC stainings, PFA-fixed cardiac tissue was washed in PBS and incubated in 15%
676 sucrose in PBS for 6-12h and 30% sucrose for 6-12h under constant rotation at 4°C
677 for cryoprotection. Cardiac tissue was frozen embedded in Tissue-Tek O.C.T.
678 Compound (Sakura Finetek) in -40°C methyl butane and stored at -80% until further
679 use. Hearts were cut into 7 µm cryosections on a Cryostat Microtome (CMC3050 S,
680 Leica Biosystems). Prior to staining, cryosections were re-hydrated in Tris-buffered
681 saline (TBS) for 10 min at RT and subsequently permeabilized in TBS with 0.1%
682 Tween 20 (TBST) for 5 min at RT. Blocking was performed with 5% bovine serum
683 albumin (BSA) and 10% normal donkey serum (NDS) in TBST for 20 min at RT.

684 For wheat germ agglutinin (WGA) staining, cryosections were incubated with WGA
685 Fluorescein (1:800, Vector Laboratories) and DAPI staining solution (1:1000, Biotium)
686 in TBST + 5% NDS for 2 h at RT. For extracellular matrix (ECM) protein staining,
687 cryosections were incubated with primary antibodies, rabbit anti-fibronectin (1:100,
688 polyclonal, abcam) and goat anti-type I collagen (1:50, polyclonal, Southern Biotech),
689 in TBST + 5% NDS overnight at 4 °C. After washing in TBST, cryosections were

690 incubated with secondary antibodies, donkey anti-rabbit IgG Alexa Fluor Plus 488
691 (1:1000, Thermo Fisher) and anti-goat IgG Alexa Fluor Plus 555 (1:1000, Thermo
692 Fisher), together with DAPI (1:1000, Biotium) in TBST + 5% NDS for 1 h at RT. After
693 washing in TBS, slides were mounted with DAKO fluorescent mounting medium.

694 Slides were imaged using the PANNORAMIC™ MIDI II digital slide scanner
695 (3DHistech) with a 20x objective. For each heart, six representative snapshots were
696 taken at 20x magnification using CaseViewer (v2.2.1, 3DHistech) for downstream
697 analysis.

698 For PSR and ECM stainings, the percentage of positively stained area was quantified.
699 Snapshots were pre-processed using Fiji to generate a binary image of stained versus
700 unstained areas, and quantification was performed using CellProfiler. For WGA
701 staining, the size of the unstained area was quantified. After pre-processing in Fiji,
702 each snapshot was segmented in Ilastik by classifying pixels as stained or unstained
703 using an interactive machine-learning algorithm. The size of segmented objects
704 (unstained areas) was subsequently quantified using CellProfiler. The mean value
705 across all snapshots was calculated per animal.

706

707 **Telemetry**

708 In a subset of mice (n= 7 STNx, n= 7 STNx Abx) subcutaneous radiotelemetry
709 transmitters (PA-C10 BP, DSI data science international, St. Paul, MN, USA) were
710 implanted one week prior to the administration of antibiotics. Due to the length of the
711 study, we measured blood pressure on a weekly 3-day period (except w2, which had
712 a 2-day measurement). Means and SD per each 3-day measurement period were
713 calculated and values with an absolute SD > 5 were excluded from downstream
714 analysis. Longitudinal curves were generated by a non-parametric, locally weighted
715 scatterplot smoothing (LOESS) regression. For statistical analysis, systolic and
716 diastolic blood pressure AUCs were computed and divided by the total elapsed
717 recording time (in minutes) to yield average blood pressure per minute. Group
718 differences were assessed using a Wilcoxon test. Of the 14 mice initially implanted
719 with radiotelemetry transmitters, 5 mice died perioperatively and were excluded. An
720 additional 3 mice were removed prior to analysis due to telemetry signal instability and
721 inconsistent blood pressure recordings. Thus, only animals that survived surgery and

722 maintained stable telemetry signals throughout the study (n=3 per group) were
723 included in the final analysis.

724

725 **Wire myography**

726 From a subset of animals (n=5 STNx, n=8 STNx + Abx), mesenteric arteries were
727 removed, immediately transferred to cold (4°C) oxygenated (95% O_2/ 5% CO_2)
728 physiological salt solution (PSS: 119 NaCl, 4.7 KCl, 1.2 KH_2PO_4, 25 $NaHCO_3$, 1.2
729 Mg_2SO_4, 11.1 glucose, and 1.6 $CaCl_2$ in mmol/L), and dissected into 2-mm rings (n=2
730 per animal). Perivascular fat and connective tissues were removed. Each ring was
731 positioned between two stainless steel wires (0.0394-mm dia.) in a 5-mL PSS-filled
732 organ bath of Small Vessel Myograph (DMT 630MA, Danish Myo Technology, Aarhus,
733 Denmark). The PSS was continuously oxygenated and kept at 37°C (pH 7.4).
734 Mesenteric rings were placed under a tension equivalent to that generated at 0.9 times
735 the diameter of the vessel at 100 mm Hg. This normalization procedure was performed
736 to obtain the passive diameter of the vessel at 100 mm Hg. The software LabChart 8
737 was used for data acquisition and display. The rings were precontracted with the KCl
738 buffer (119 NaCl, 60 KCl, 1.2 KH_2PO_4, 25 $NaHCO_3$, 1.2 Mg_2SO_4, 11.1 glucose, and
739 1.6 $CaCl_2$ in mmol/L) and equilibrated until a stable resting tension was acquired. To
740 test the endothelial function, vessels were precontracted with 1 µmol/L phenylephrine.
741 After all vessel segments had reached a stable contraction plateau, increasing doses
742 of acetylcholine were administered to the organ baths (3 to 1000 nmol/L). Tension is
743 expressed as a percentage of the steady-state tension (100%) obtained with
744 phenylephrine.

745

746 **Immunophenotyping**

747 <u>Plasma collection, immune cell isolation and flow cytometry measurements</u>

748 Whole blood was collected in lithium-heparin syringes (80 IU/3 mL, BD Vacutainer A-
749 Line) for anticoagulation and centrifuged at 1,500 g for 15 min at RT. Plasma was
750 collected and frozen at -80 °C, and the remaining blood cell pellet was resuspended
751 in erythrocyte lysis buffer (83 g/L NH_4Cl, 8.5 g/L $NaHCO_3$, 10 mM EDTA) and
752 incubated at 37 °C for 6 min for peripheral blood cell (PBC) isolation. After
753 centrifugation at 400 g for 5 min (RT), supernatant was discarded and cells underwent

754 a second erythrocyte lysis step (37 °C, 4-6 min). Reaction was stopped using ice-cold
755 PBS + 0.5 % BSA + 2 mM EDTA (referred to as FACS buffer) and cell suspension was
756 filtered through a 30 µm strainer.

757 Spleens were excised and kept in FACS buffer at 4 °C. Single cell suspensions were
758 obtained by pressing tissue through 70 µm EasyStrainer, followed by erythrocyte lysis
759 and filtration through 40 µm EasyStrainer.

760 Hearts were excised, atria were removed and tissue was kept in HBSS without
761 Ca^{2+}/Mg^{2+} + 10 mM HEPES (referred to HBSS w/o) at 4 °C. Ventricles were cut into 2-
762 3 mm pieces before transfer into gentleMACS C Tubes (Miltenyi Biotec). A fresh
763 digestion mix was prepared with DNase I (30 U/mL), Hyaluronidase I-S (60 U/mL),
764 Collagenase XI (125 U/mL) in 1 mL HBSS with Ca^{2+}/Mg^{2+}. Samples were incubated
765 for 1 h at 700 rpm and 37 °C, followed by mechanical dissociation using the
766 gentleMACS Octo Dissociator (Miltenyi Biotec, program m_heart_02). Digestion was
767 quenched using ice-cold PBS + 10 % FBS. Cells were pelleted (400 g, 10 min, 4 °C),
768 treated with erythrocyte lysis buffer for 3 min at RT, neutralized with FACS buffer, and
769 filtered sequentially through 70 µm and 40 µm EasyStrainers. An aliquot was collected
770 for absolute counting (1:100 dilution).

771 Intestines were excised, flushed with HBSS w/o to remove all contents, divided into
772 small intestine (duodenum, jejunum, ileum) and large intestine (cecum, colon) and
773 stored in HBSS w/o at 4 °C. Lamina propria cells were isolated using the Lamina
774 Propria Dissociation Kit, mouse (Miltenyi Biotec).

775 Heart and lamina propria cell suspensions were subjected to a 40%/80% Percoll
776 density gradient (centrifugation at 800 g, 20 min, RT, no brake). Immune cells were
777 harvested at the interphase and washed in FACS buffer.

778 Splenocyte and lamina propria cell suspensions were counted on a LUNA-FL Dual
779 Fluorescence Cell Counter (Logos Biosystems), centrifuged and resuspended at
780 $1x10^6$ cells per 100 µL medium (RPMI 1640 + 10% FBS + 1% penicillin/streptomycin
781 [P/S, 10,000 U/mL / 10,000 µg/mL]) for further analysis. PBC and heart cell
782 suspensions were directly centrifuged and resuspended in 100 µL medium per flow
783 cytometry panel.

784 Cells were either immediately stained for flow cytometry or restimulated with 50 ng/mL
785 PMA, 500 ng/mL ionomycin, and 0.75 µL/mL GolgiStop in medium for 4 h at 37 °C, 5 %

786 CO_2. Viability was assessed with Live/Dead Fixable Aqua for 405 nm (Thermo Fisher),
787 surface markers were stained in Brilliant Stain Buffer (BD Biosciences) with Fc block
788 (Miltenyi Biotec), then cells were fixed/permeabilized (eBioscience
789 FoxP3/Transcription Factor Buffer Kit) for intracellular staining. All antibody
790 incubations were 30 min at 4 °C (Table S7). Data were acquired on a BD LSRFortessa
791 with high throughput sampler (HTS) using BD FACSDiva and analyzed in
792 FlowJo 10.8.1.

793

794 Flow cytometry analysis

795 Immune cell populations were identified by flow cytometry using the gating strategies
796 in Figure S9. For the immune cell abundance analysis, batch effects arising from
797 different flow cytometry acquisition days were corrected using ComBat from the *sva* R
798 package (v.3.20). Raw abundance values were imported into R and the matrix of cell-
799 type frequencies was extracted. Batch identifiers were supplied as the batch variable,
800 and group assignment was included as a covariate in the ComBat model matrix.
801 ComBat was run with parametric priors and without generating prior plots, yielding
802 batch-adjusted abundance values that were re-combined with sample metadata for
803 downstream analyzes. All subsequent analyzes were performed on the batch-
804 corrected dataset using the same gating-based cell populations described above.
805 UMAP visualizations were generated from the T-cell panel using two representative
806 samples per group. $CD3^+$ T cells were isolated using the hierarchical gating strategy,
807 and all gated events (10,000 $CD3^+$ T cells per sample) were used for dimensionality
808 reduction. UMAP embeddings were computed in FlowJo using the UMAP_R plugin
809 (version 4.1.1) with Euclidean distance, minimum distance = 0.1, and 15 nearest
810 neighbours. FlowJo's default logical transformation was applied to all fluorescence
811 channels. Group-level embedding intensity plots were created in FlowJo by overlaying
812 all cells from the same group and visualizing them as smoothed density distributions.

813

814 **Mouse AhR reporter assay**

815 Mouse AhR-responsive reporter cell line (H1L1.1c2), derived from mouse hepatoma
816 (Hepa1c1c7) cells and stably transfected with the pGudLuc1.1 vector containing AhR-
817 responsive dioxin response elements (DRE) upstream of a luciferase gene, was kindly

818 provided by Prof. Michael S. Denison, University of California, Davis, CA, USA.
819 H1L1.1c2 cells were cultured in Opti-MEM (Thermo Fisher, 31985070) supplemented
820 with 1% FBS (Merck, F7524), 1% P/S, and 0.2 mg/mL G418 (Sigma, A1720-1G), and
821 maintained at 37 °C with 5% CO_2. Subculture was performed twice a week using
822 TrypLE™ Express Enzyme (Gibco, 12604-02).

823 For the assay, cells were seeded in 96-well plates at a density of $7.5x10^4$ cells/well
824 and allowed to attach for 24 h. Cells were then incubated with 10% mouse plasma in
825 the same medium for 24 h. Assays were performed in triplicate, and 6-formylindolo[2-
826 b]carbazole (FICZ) was included as a positive control at a concentration of 10 nM.
827 After treatment, luciferase activity and cell viability were quantified using the One-
828 Glo™ + Tox Luciferase Reporter and Cell Viability Assay (Promega, E7120) according
829 to the manufacturer's instructions. Luminescence and fluorescence were measured
830 using a microplate reader (Infinite 200 plate reader, Tecan). Luminescence values
831 were normalized to cell viability (fluorescence signal) and subsequently expressed
832 relative to the FICZ control within each plate.

833

834 **T_H17 polarization assay, murine**

835 Mesenteric and peripheral lymph nodes (LN) were harvested from 129S2/SvPasOrlRj
836 mice and kept in cold FACS Flow buffer. LN were mechanically dissociated through a
837 70 µm cell strainer using cold FACS Flow buffer. The cell suspension was
838 subsequently filtered through a 40 µm strainer, washed with 20 mL FACS Flow buffer,
839 and centrifuged at 400 × g for 10 minutes at 4°C. Cells were resuspended in FACS
840 Flow buffer at 1 × 10^7 cells per 100 µL.

841 CD4+ T cells were enriched via magnetic-activated cell sorting (MACS) using the
842 MojoSort Mouse CD4 T Cell Isolation Kit (BioLegend) with minor modifications for the
843 use of magnetic columns. Briefly, cells were incubated with a biotinylated antibody
844 cocktail (2 µL per 10^7 cells in 100 µL) for 15 minutes at 4°C, followed by Streptavidin
845 Nanobeads (2 µL per 10^7 cells) for an additional 15 minutes at 4°C. Cells were
846 separated using LS columns (Miltenyi Biotec) and the unlabelled fraction was used for
847 further analysis. For naïve CD4+ T cell isolation, cells were stained with CD4
848 (VioGreen), CD25 (PE), CD44 (BB700), CD62L (BV421), and a live/dead stain

849 (Zombie Green) and $CD4^{+}CD25^{-}CD44^{low}CD62L^{high}$ cells were sorted on a FACS
850 Melody (BD Bioscience, 100 µm nozzle).

851 96-well flat-bottom plates were coated overnight at 4°C with anti-CD3 antibody (2
852 µg/mL in PBS, 50 µL per well). Naïve CD4+ T cells were resuspended in T_H17
853 differentiation medium (RPMI-1640 supplemented with 10% FCS, 1% penicillin-
854 streptomycin, 1% L-glutamine, 1% non-essential amino acids, 1 mM sodium pyruvate,
855 and 0.01 mM β-mercaptoethanol). Cells were plated at 5 × 10^4 cells per well in a final
856 volume of 200 µL with anti-CD28 (2 µg/mL), mIL-6 (80 000 U/mL, Miltenyi Biotec),
857 rhTGFβ1 (40 U/mL, Miltenyi Biotec) and mIL-1β (33 600 U/mL, Miltenyi Biotec) and
858 test compounds (IxS, KCl, AhRi at concentrations indicated in the respective figure) or
859 DMSO vehicle control, as appropriate. Cells were cultured at 37°C with 5% CO_2 for 4
860 to 5 days and subsequently restimulated for 4 hours with PMA (50 ng/ mL), ionomycin
861 (750 ng/mL), and GolgiPlug (0.5 µL/mL). Following restimulation, cells were washed
862 with FACS Flow buffer, stained with BD Horizon Fixable Viability Stain 700 (1:500
863 dilution) for 30 minutes cold, fixed, and permeabilized using Fix/Perm buffer
864 (eBioscience), and stained with the antibodies indicated in Table S7. Cells were
865 analyzed using a BD LSRFortessa with high throughput sampler (HTS). Data were
866 processed using FlowJo.

867

868 **RNA isolation**

869 Splenocytes were isolated as described above, enriched for CD45+ using mouse
870 CD45 MicroBeads (Miltenyi Biotec). Hearts were excised and apex was snap frozen
871 at -80°C. Spleens were excised and a small piece of tissue was placed into 300 µL
872 RNAprotect Tissue Reagent (Qiagen) at 4 °C for a minimum of 24 h. RNAprotect
873 Tissue Reagent was then discarded, and tissues were frozen at -80 °C.

874 RNA isolation from splenocytes and spleen was performed using the RNeasy Mini Kit
875 (Qiagen). RNA isolation from heart was performed using the RNeasy Fibrous Tissue
876 Mini Kit (Qiagen). For cell homogenisation, enriched CD45+ splenocytes were
877 resuspended in buffer RLT + β-mercaptoethanol and vortexed vigorously. Tissue
878 pieces were immersed in RLT buffer + β-mercaptoethanol with 1.5 mm ceramic beads
879 and placed into a Precellys 24 tissue homogeniser. RNA was subsequently isolated
880 from both sample types according to the instructions of the respective kits.

881 Fibroblasts on well plates were washed in PBS and incubated with 700 µL Qiazol Lysis
882 Reagent (Qiagen) per well at -80 °C over night. Then, lysed cells were harvested,
883 transferred to a tube and vortexed vigorously. 200 µL of chloroform was added and
884 samples were centrifuged at 12,000 g for 15 min at 4 °C. Afterwards, the aqueous
885 phase was collected and RNA was isolated with the RNeasy Mini Kit according to the
886 manufacturer's protocol.

887

888 **Quantitative polymerase chain reaction (qPCR)**

889 All qPCR was performed on a QuantStudio™ 5 Real-Time PCR System (Thermo
890 Fisher Scientific) using a 384-well plate format. For each 5-µL reaction mix, 4 ng of
891 DNA or cDNA was used, and all detections were performed in triplicate. All primer and
892 probe sequences and concentrations are listed in Table S6.

893 For all SYBR-Green based detection, the PowerUP™ SYBR™ Green Master Mix
894 (Thermo Fisher Scientific) was used with a fast cycling protocol of 50 °C for 2 min, 95
895 °C for 2 min, followed by 40 cycles of 95 °C for 1 s and 60 °C for 30 s. For all TaqMan-
896 based detection, the TaqMan® Multiplex Master Mix (Thermo Fisher Scientific,
897 4461882) was used with a fast cycling protocol of 95 °C for 20 s, followed by 40 cycles
898 of 95 °C for 2 s and 60 °C for 20 s.

899 For *16S* quantification, cecal DNA was amplified and detected using SYBR Green and
900 the standard curve method. Standard curves were generated using 10-fold serial
901 dilutions ranging from 10^1 to 10^9 copies of the *16S* rRNA gene of *E. coli* (Invitrogen)
902 amplified with primers 27F (5′-GTTTGATCCTGGCTCAG-3′) and
903 1492R (5′-CGGCTACCTTGTTACGAC-3′). Using the resulting curve, *16S* rDNA copy
904 numbers per gram content were calculated.

905 For all other genes, cDNA was synthesized prior to qPCR using the High Capacity
906 cDNA Reverse Transcription Kit (Thermo Fisher Scientific). Murine *Col1a2*, *Acta2*,
907 *Cyp1a1* and *18s* were detected using TaqMan. Gene expression was normalized to
908 the *18s* signal using the ΔΔCt method. All other murine genes were quantified using
909 SYBR Green, and *Hprt* or *Gapdh* as the housekeeping genes. All human genes were
910 quantified using SYBR Green and normalized to *HPRT1* using the ΔΔCt method. All
911 primer and probes are shown in Table S6.

912 **Bulk mRNA sequencing**

913 Illumina stranded mRNA library preparation and bulk mRNA sequencing were
914 performed at the BIH/MDC Genomics Technology Platform. Paired-end sequencing
915 was performed on an Illumina NovaSeq X Plus platform, targeting ~30 million reads
916 per sample. Transcript quantification of raw sequencing data to the *Mus musculus*
917 reference transcriptome (GRCm38) was performed using Salmon (v1.10.1). Quality
918 assessment of the preprocessing was performed using MultiQC (v1.6). Following
919 quality control, 26.4M-34.7M paired-end reads per sample were retained and included
920 in downstream analysis. Gene symbols were generated from Ensembl gene IDs using
921 biomaRt (v2.52.0, Ensembl release 102). Post-processing quality control and
922 downstream data analysis were conducted using DESeq2 (v1.42.1).

923 For the Abx trial, separate DeSeq2 datasets were generated for each reference
924 condition (Sham, STNx). Lowly expressed genes were removed by filtering for
925 transcripts with at least 1 count per million in a minimum of two samples using edgeR
926 (v4.0.16). Differential expression analysis was performed using the DeSeq2 pipeline.
927 Log_2 fold changes were adjusted using lfcShrink with the ashr method (v2.2.63), and
928 p-values were corrected using a false discovery threshold of 10%. Variance-stabilized
929 expression values were obtained using the rlog transformation.

930 Gene set enrichment analysis (GSEA) was performed on the overlap of significantly
931 regulated genes from the STNx vs. Sham and STNx Abx vs. STNx comparisons
932 (adjusted p-value < 0.1). Curated *Mus musculus* gene sets were downloaded from
933 MSigDB. Enrichment was calculated with Fisher's exact test and FDR correction,
934 using all Ensembl gene IDs present in the complete MSigDB *Mus musculus* dataset
935 as the background. Pathways and GO terms not relevant to the study were excluded
936 from visualisation using targeted keyword filtering.

937 For the AhRi trial, differential expression analysis with DeSeq2 was restricted to the
938 set of DEGs in STNx that were Abx responsive. Batch effects between experimental
939 rounds were corrected using ComBat-seq (sva, v3.50.0). Genes significantly regulated
940 by AhRi-treatment in the same direction as the Abx-dependent response (p < 0.1)
941 were subjected to GSEA.

942 For both trials, targeted gene set variation analysis (GSVA) was performed on rlog-
943 transformed expression values using curated gene sets relevant to the T_H17 axis (gsva
944 package, v1.50.5).

945

946 **Single-cell RNA-sequencing**

947 We analyzed publicly available mouse cardiac single-nucleus and human single-cell
948 RNA-seq datasets[32,37]. Processed Seurat objects were imported into R (v4.2.2) using
949 Seurat (v5.0). No reclustering or reannotation was performed. For each dataset, cells
950 belonging to diseased samples (mouse CKD or human CKD) and appropriate controls
951 were subset for downstream analyzes. Resident structural cell types were selected
952 based on the original annotations, and expression of IL17ra was quantified from log-
953 normalized RNA values to identify positive and negative stromal populations.
954 Extracellular matrix (ECM) activity was assessed using an extended NABA matrisome
955 gene list[33] and compared using Wilcoxon tests. AhR pathway activity was similarly
956 scored using a recently published AhR-responsive gene set[60]. Differential expression
957 was performed using the MAST framework[61], including only genes expressed in more
958 than 10% of nuclei. Genes were considered differentially expressed when meeting:
959 adjusted $p < 0.1$, absolute $\log_2$ fold change > 0.3, and average normalized expression
960 > 3 in Il17ra$^+$ cells. Differentially expressed genes were compared with curated
961 fibroblast transcriptional signatures derived from human cardiac and stromal
962 datasets[34] to identify enriched transcriptional programs. Briefly, DEG were intersected
963 with each fibroblast signature and the number of overlapping genes, proportion of
964 signature genes present among upregulated genes, and average FC and expression
965 of the overlapping genes were used to find similar transcriptional programs. Cytokine-
966 response enrichment was conducted from DEG of cardiac lymphocytes as described
967 above using the Immune Response Enrichment Analysis (IREA)[62] software.

968

969 **Murine cardiac fibroblasts**

970 Hearts were freshly harvested from 7-10 weeks old male and female C57BL/6J mice
971 and rinsed twice in PBS. Aortic and atrial tissues were removed, and ventricles were
972 minced and transferred into 1 mL of enzymatic digestion solution containing DNase I
973 (300 U/mL), Hyaluronidase I-S (60 U/mL), Collagenase XI (125 U/mL), and

974 Collagenase I (450 U/mL) in DMEM. Digestion was performed on a shaking incubator
975 (800 rpm, 37 °C) for 45 minutes.

976 Following digestion, the cell suspension was filtered through a 70 µm strainer using
977 PBS and centrifuged at 400 g for 10 minutes at 37 °C. The pellet was resuspended in
978 1 mL erythrocyte lysis buffer (Erylysis), incubated for 3 minutes at RT, and quenched
979 with PBS. Cells were centrifuged again under the same conditions, supernatant was
980 discarded, and the pellet was resuspended in 4 mL fibroblast culture medium (DMEM
981 supplemented with 20% FBS, 2% penicillin-streptomycin, 1 ng/mL endothelial cell
982 growth factor [ECGF], and 10 µg/mL heparin). Cells were maintained at 37 °C and 5%
983 CO_2. Media was changed after 2.5 h and further replaced every 2-3 days. For
984 subculture, fibroblasts were detached using Trypsin-EDTA (1mL, 2-3 min incubation).
985 Reaction was stopped with culture media, fibroblasts were transferred to a 15 mL tube
986 and centrifuged at 400 g for 10 min. Pellet was resuspended in culture media, counted
987 and plated into tissue flasks or well plates depending on cell counts (6.000-10.000
988 cells/cm^2).

989 Assay was performed on a 6-well plate. In brief, fibroblasts were starved in culture
990 media containing 1% FBS and incubated for 4 h at 37 °C, followed by a 24 h incubation
991 with the test substances. Murine recombinant IL-17A was used at 1 ng/mL in culture
992 media. Potassium 3-indoxyl sulfate was used at 50 µM and 100 µM on its own, and at
993 100 µM in combination with IL-17A in culture media. After 24 hours incubation,
994 fibroblasts were washed in PBS and incubated with 700 µL Qiazol Lysis Reagent per
995 well at -80 °C over night. Lysed fibroblasts were then harvested, RNA was isolated
996 and RT-qPCR was performed as described above.

997 For immunofluorescence staining, 18x18 mm coverslips were sterilized with ethanol
998 70% and placed into 6-well plates. Fibroblasts were grown on the coverslips in culture
999 media until desired confluence. Cells were then washed with PBS and fixed with 4%
1000 Paraformaldehyde, followed by permeabilization with 0.1% Triton X-100 and blocking
1001 with 10% normal donkey serum (NDS) in PBS.

1002 For PDGFRα and VIM staining, cells were incubated with conjugated antibodies (anti-
1003 mouse CD140a PE, 1:100, clone APA5, Miltenyi, 130-102-502 and AF647 anti-
1004 vimentin, 1:500, clone EPR3776, ab194719) for 2 h at RT in PBS + 10% NDS. For
1005 COL-1 and IL17RA staining, cells were incubated with primary antibodies (goat anti-

type I collagen, 1:500, polyclonal, Southern Biotech, 1310-01 and rabbit anti-IL17RA, 1:500, polyclonal, abcam, ab180904) for 2 h at RT in PBS + 10% NDS. After washing with PBS + 1% NDS, secondary antibodies, donkey anti-rabbit IgG Alexa Fluor Plus 488 (1:1000, Thermo Fisher) and anti-goat IgG Alexa Plus 555 (1:1000, Thermo Fisher), were incubated together with DAPI (1:1000, Biotium) in PBS + 10% NDS for 1 h at RT. After washing, coverslips were taken out of the well plates and mounted onto microscopy slides using DAKO fluorescent mounting medium. Slides were imaged on the Keyence Compact Fluorescence microscope with the Plan Apochromat 20x objective lens.

For flow cytometry staining, cells were stained for PDGFRα, CD45 and CD31 (antibody concentrations in Table S7) together with SYTOX™ Green Dead Cell Stain (1:500, Invitrogen, S34860) and Fc blocking reagent (Miltenyi Biotec, 130-092-575) in FACS buffer. Data were acquired on a BD LSRFortessa using BD FACSDiva and analyzed in FlowJo 10.8.1.

Splenocyte incubation assay

Spleens from 129S2/SvPasOrlRj mice were processed to obtain spleen single-cell suspensions as described above. For *ex vivo* stimulation, splenocytes were incubated for 4 h at 37 °C, 5 % CO_2 in RPMI-1640 in the presence of IxS and AhRi at the indicated concentrations. After incubation, cells were resuspended in buffer RLT + β-mercaptoethanol and frozen at −80 °C for subsequent RNA isolation as described above.

Patient serum collection

Patients with CKD stage 5 dependent on hemodialysis were recruited Department of Nephrology and Medical Intensive Care at Charité-Universitätsmedizin Berlin. Healthy volunteers were recruited at the Experimental and Clinical Research Center (ECRC) of Charité-Universitätsmedizin Berlin. Ethical approval was obtained from the institutional review board of Charité–Universitätsmedizin Berlin (EA2/162/17) and all participants provided written informed consent before biomaterial was collected. Blood was obtained from patients at the start of hemodialysis. Serum was collected by

1037 centrifugation at 1500 g for 15 min at RT, and stored at -80 °C until further use.
1038 Demographic and clinical characteristics of the study cohort are summarized in Table
1039 S4.

1040

1041 **Human luciferase reporter assay**

1042 Human AhR reporter cell line (HT29-Lucia™ AhR, InvivoGen, ht21-ahr), containing
1043 AhR-responsive DRE upstream of a Lucia luciferase gene, was cultured in Dulbecco's
1044 Modified Eagle Medium (DMEM) supplemented with 10% FBS and 100 µg/mL Zeocin
1045 (InvivoGen, ant-zn-05), maintained at 37 °C with 5% CO_2. Cells were subcultured once
1046 per week using a standard Trypsin-EDTA protocol and partially replenished with fresh
1047 medium mid-week between passages.

1048 For the assay, 180 µL of cell suspension per well was seeded on a 96-well plate at a
1049 density of 2.8×10^5 cells/mL in medium without Zeocin. For the dose-response curve of
1050 AhRi, cells were incubated with 100 µM IxS and AhRi concentrations between 1 nM
1051 and 10 µM or VEH (vehicle, DMSO content of the highest AhRi concentration) for 24
1052 h in quadruples. To assess the AhR activation potential of human biomaterial, cells
1053 were incubated with 10% patient serum and AhRi in a final concentration of 1 or 0.1
1054 µM, or VEH for 24 h in triplicates. For quantification, 20 µL of culture supernatant was
1055 used to determine luciferase activity using the QUANTI-Luc™ Luciferase Detection
1056 Reagent (InvivoGen, rep-qlc4lg1). Luminescence was measured using a microplate
1057 reader (Infinite 200 plate reader, Tecan).

1058

1059 **Human T_H17 polarization assay**

1060 Peripheral blood mononuclear cells (PBMC) were collected together with serum from
1061 healthy volunteers under the ethics approval described above (EA2/162/17). PBMC
1062 were isolated from EDTA-anticoagulated blood of a healthy donor by diluting samples
1063 1:1 in PBS + 2% FBS and layering them into 50 mL SepMate tubes (Stemcell) prefilled
1064 with 15 mL Pancoll (PAN Biotech). After centrifugation at 1200 g for 10 min at RT, the
1065 mononuclear cell layer was collected, transferred into a fresh 50 mL tube, and washed
1066 with PBS + 2% FBS, followed by erythrocyte lysis.

1067 T cells were isolated from PBMC using MojoSort Human CD4 T Cell Isolation Kit
1068 (Biolegend) with LS columns (Miltenyi) following the manufacturer's protocol. To obtain
1069 naïve CD4 cells, the enriched T helper cell fraction was sorted using a BD FACSAria
1070 III (BD Bioscience, 70 µm nozzle) by staining for CD4, CD25, CD127, CD45RO (Table
1071 S8), and dead cells exclusion with DRAQ7 (1:250, Miltenyi Biotec).

1072 Naïve CD4 T cells were resuspended in X-VIVO 15 serum-free hematopoietic media
1073 (Lonza Bioscience) and plated at $5x10^4$ cells per well in anti-CD3-coated (10 µg/mL,
1074 BD) 96-well U-bottom plates and 1 µg/mL anti-CD28 (BD). To induce T_H17
1075 polarization, naïve CD4 T cells were cultured with 12.5 ng/mL IL-1β, 25 ng/mL IL-6,
1076 25 ng/mL IL-21, 25 ng/mL IL-23, and 5 ng/mL TGF-β (all Miltenyi Biotec), while T_H0
1077 control wells were left without cytokine supplementation. Cells were treated with 2.5%
1078 serum from either hemodialysis patients or healthy controls in triplicates and
1079 maintained for 7 days at 37°C and 5% CO2.

1080 Prior to analysis, cells were restimulated for 4 h with 10 ng/mL PMA (Merck), 500
1081 ng/mL ionomycin (Merck), and 1 µL/mL GolgiPlug (BD), stained with LIVE/DEAD
1082 fixable aqua dye (Invitrogen), fixed and permeabilized using the Foxp3/Transcription
1083 Factor Staining Buffer Set (Invitrogen), and finally stained with antibody panels with
1084 Fc Block, CD4 and IL-17A (antibodies listed in Table S8).

1085 Cells were analyzed using a BD LSRFortessa with HTS and data were processed
1086 using FlowJo (v10.10).

1087

1088 **UK Biobank**

1089 Study participants

1090 The UK Biobank is a population-based cohort of 502,366 participants aged 40-69
1091 years recruited between 2006 and 2010 across 22 assessment centers in England,
1092 Scotland, and Wales. Ethical approval was granted by the North West Multi-Centre
1093 Research Ethics Committee (reference 11/NW/0382), and all participants provided
1094 written informed consent. Data available as of 16 November 2023 were used for this
1095 study.

1096 Participants with impaired kidney function were defined as those with an estimated
1097 glomerular filtration rate (eGFR) below 60 mL/min/1.73 m², corresponding to KDIGO

categories G3-G5. Demographic and clinical characteristics of the study cohort are summarized in Table S5.

Identification of individuals with heart failure with preserved ejection fraction (HFpEF) followed a previously published multi-stage algorithm[63]. All HFpEF cases were required to exhibit at least one clinical symptom of heart failure in accordance with European Society of Cardiology (ESC) guidelines, supplemented by additional criteria depending on data availability. When cardiac magnetic resonance (CMR) imaging was available, participants with a left ventricular ejection fraction above 49% were considered to have preserved systolic function. When NT-proBNP measurements were available, patients exceeding the 90th percentile were classified as HFpEF, whereas those with lower values or evidence of reduced ejection fraction were excluded. For participants lacking imaging or proteomic data, HFpEF was assigned when the pre-test probability exceeded 90%.

Data modalities

All variables used in this study were assessed prior to or at the baseline visit. eGFR was calculated from plasma cystatin C concentrations using the equation eGFR = 74.835 / (cystatin $C^{1.333}$). Albuminuria was quantified as the urine albumin-to-creatinine ratio. Essential hypertension was defined by the presence of an ICD-10 I10 diagnosis code recorded before baseline. Proteomics profiling was available for approximately 10% of the UK Biobank participants and was performed using Olink proximity extension assays, with protein concentrations reported as $\log_2$-normalized protein expression (NPX) values. For the present analysis, we focused on NT-proBNP and IL-17A, which were available for 51,578 and 50,573 participants, respectively. Smoking exposure was quantified using the UK Biobank variable “pack years of smoking” (Field-ID 20161), calculated from baseline questionnaire responses using the formula: (cigarettes per day / 20) * (age stopped smoking - age started smoking). This measure reflects cumulative smoking intensity, with higher values reflecting greater lifetime exposure.

Statistical Analysis

Time-to-event outcomes were evaluated using Kaplan-Meier estimators implemented in the Python package lifelines (version 0.30.0). Participants were stratified into three IL-17A groups according to the plasma IL-17A concentrations: below the 25th

1130 percentile, between the 25th and 75th percentiles, and above the 75th percentile.
1131 Survival time was defined as the interval from baseline to the occurrence of the event
1132 of interest, with censoring at the end of follow-up. Differences across IL-17A strata
1133 were assessed using the log-rank test.

1134 To evaluate the association between IL-17A and clinical outcomes, Cox proportional
1135 hazards models were fitted. All covariates were standardized before model fitting to
1136 facilitate direct comparison of effect sizes. Cox proportional hazards models were
1137 estimated using an unpenalized framework with robust variance estimation. To ensure
1138 numerical stability, a limited grid of ridge penalisation terms ($\lambda = 0$ to 0.01) was
1139 evaluated, and the model yielding stable convergence without materially influencing
1140 effect estimates was selected. Hazard ratios (HRs) and 95% confidence intervals (CIs)
1141 were derived from the final model and displayed using forest plots.

1142 Normality of continuous variables was assessed using the Shapiro-Wilk test. When
1143 both groups satisfied the normality assumption ($p > 0.05$), differences were evaluated
1144 using Welch's *t* test; otherwise, comparisons were performed using the non-parametric
1145 Mann-Whitney U test. For analyzes involving multiple statistical tests, p-values were
1146 adjusted using the Benjamini-Hochberg false discovery rate (FDR) procedure. All
1147 statistical analyzes were performed in Python 3.11.

1148

1149 **Human cardiac fibroblasts**

1150 Human cardiac fibroblasts were obtained from PromoCell (Germany). Cells were
1151 seeded (4000 cells per cm^2 seeding density) with 18 mL of Fibroblast Growth
1152 Medium 3 (PromoCell, Germany) into a tissue flask T75. Media contained
1153 supplements (PromoCell, Germany), P/S (1%) and Amphotericin B (Gibco, 0.2%).
1154 Cells were maintained at 37 °C and 5% CO_2 with medium exchanged every 2-3 days
1155 and passaged at 70-90% confluence as described above. Subculture was performed
1156 using the standard Trypsin-EDTA protocol.

1157 For all experiments, cells were seeded at manufacturer recommended densities and
1158 allowed to attach overnight. The following day, cultures were starved for 4h in medium
1159 containing 1% FBS and subsequently stimulated for 24h under the appropriate
1160 conditions. Treatments included IL-17A (1 ng/mL), IxS (100 µM), AhRi (1 µM),
1161 Secukinumab (Cosentyx, 10 nM), human serum (HD/HC; 10%), or the corresponding

1162 combinations. After stimulation, cells were washed once with PBS and lysed in QIAzol
1163 as descrived above. Lysed cells were then harvested, RNA was isolated and RT-
1164 qPCR was performed as described above.

1165 To assess viability and proliferation, fibroblasts were co-incubated with IL-17A and IxS
1166 in starved medium for 24 h. After detaching, cells were stained with Zombie Green
1167 Fixable Viability Kit (1:500, BioLegend), fixed/permeabilized (eBioscience
1168 FoxP3/Transcription Factor Buffer Kit) for intracellular staining, and stained for Ki-67
1169 (Table S8.)

1170

1171 **Data and code availability**

1172 All code, data, and scripts used in this study will be made publicly available. The code
1173 and scripts will be made accessible on Zenodo. The raw sequencing data will be
1174 deposited in the NCBI Sequence Read Archive.

Author contribution

CRediT: Conceptualization: AY, WA, AT, JH, HB, NW; Data curation: AY, WA, JVe, HA, MK; Formal Analysis: AY, WA, OP; Funding acquisition: VM, UK, AZ, PO, WG, KUE, DNM, MK, HB, NW; Investigation: AY, WA, AT, OP, FS, IAS, AMR, JVe, NG, VM, SH, SK, GT, HA, FF, CH, SAH, PMB, MIW, FB; Methodology: AY, WA, OP, FS, IAS, JVe, JVo, PO, WG, KD, MK, HB, NW; Project administration: AY, WA; Resources: UK, TK, BK, AZ, PO, WG, KD, KUE, DNM, MK, JH, HB, NW; Software: AY, WA, JVe, HA; Supervision: JVo, UK, TK, BK, AZ, PO, WG, KD, KUE, DNM, MK, JH, HB, NW; Validation: AY, WA, RK, MK; Visualization: AY, WA, JVe, HB, NW; Writing - original draft: AY, WA, HB, NW; Writing - review & editing: all authors.

Acknowledgment

We thank Melanie Röhr and Gudrun Koch for their technical assistance, Ilona Kamer for the implantation of the blood pressure telemetry devices and Heike Schwede for support with animal husbandry. We also thank Laura Mossier for contributing to the HFpEF trial, and Daniel Herrmann for his technical assistance with the IxS quantification. Clinical chemistry and echocardiography measurements were performed at the Preclinical Research Center of the MDC. Bulk mRNA-seq was performed at the BIH/MDC Genomics Technology Platform. Human T cells were sorted using the flow cytometry platform of the MDC. We thank the MDC Max Cluster for providing us with the scientific compute cluster resources and Ulrike Löber for bioinformatics support.

Funding

FACSMelody used in this study was funded by German Federal Ministry of Research, Technology and Space (BMFTR), project-ID: 01EJ2202A. V.M., D.N.M., W.G., S.K., P.J.O., H.B., and N.W. were supported by the BMFTR, TAhRget consortium (project-ID 01EJ2502A (N.W.), 01EJ2502B (W.G., S.K., and P.J.O.), 01EJ2502E (V.M., D.N.M.), and 01EJ2502G (H.B.)), as well the QEED consortium (project-ID 13N16386, to H.B.). U.K., D.N.M., A.Z. and N.W. were supported by the German Research Foundation (DFG), CRC1470 (project-ID 437531118, subproject A10 to N.W., A06 to D.N.M., and A09 to U.K.), and CRC1525 (project-ID 453989101, to A.Z.) and project-

ID 432915089 (to A.Z). D.N.M. and N.W. were supported by the DZGIF (DZG Innovation Fund), Topic “Microbiome”. K.D., W.G., S.H., and P.J.O. were supported by the German Research Foundation (DFG), project number 509149993, TRR 374. N.W. was supported from the European Research Council (ERC) under the European Union’s Horizon 2020 research and innovation program (852796). N.W. was supported by the Corona Foundation in the German Stifterverband (S199/10080/2019). K.U.E. received funding from the European Union’s Horizon 2020 research and innovation program under a Marie Skłodowska-Curie Innovative Training Networks (H2020-MSCA-ITN-2019) grant (TrainCKDis, project-ID 860977).

Conflict of interest

The authors declare no conflict of interest.

References

1 Langenberg, C., Hingorani, A. D. & Whitty, C. J. M. Biological and functional multimorbidity—from mechanisms to management. *Nature Medicine* **29**, 1649-1657 (2023). https://doi.org/10.1038/s41591-023-02420-6

2 Evenepoel, P., Poesen, R. & Meijers, B. The gut-kidney axis. *Pediatr Nephrol* **32**, 2005-2014 (2017). https://doi.org/10.1007/s00467-016-3527-x

3 Eckardt, K.-U. *et al.* Evolving importance of kidney disease: from subspecialty to global health burden. *The Lancet* **382**, 158-169 (2013). https://doi.org/10.1016/S0140-6736(13)60439-0

4 Mishima, E. *et al.* Evaluation of the impact of gut microbiota on uremic solute accumulation by a CE-TOFMS–based metabolomics approach. *Kidney International* **92**, 634-645 (2017). https://doi.org/https://doi.org/10.1016/j.kint.2017.02.011

5 Mair, R. D., Sirich, T. L., Plummer, N. S. & Meyer, T. W. Characteristics of Colon-Derived Uremic Solutes. *Clin J Am Soc Nephrol* **13**, 1398-1404 (2018). https://doi.org/10.2215/cjn.03150318

6 Jankowski, J., Floege, J., Fliser, D., Böhm, M. & Marx, N. Cardiovascular Disease in Chronic Kidney Disease. *Circulation* **143**, 1157-1172 (2021). https://doi.org/doi:10.1161/CIRCULATIONAHA.120.050686

7 Speer, T., Dimmeler, S., Schunk, S. J., Fliser, D. & Ridker, P. M. Targeting innate immunity-driven inflammation in CKD and cardiovascular disease. *Nature Reviews Nephrology* **18**, 762-778 (2022). https://doi.org/10.1038/s41581-022-00621-9

8 Wilck, N. *et al.* Salt-responsive gut commensal modulates T(H)17 axis and disease. *Nature* **551**, 585-589 (2017). https://doi.org/10.1038/nature24628

9 Granados, J. C. *et al.* AHR is a master regulator of diverse pathways in endogenous metabolism. *Scientific Reports* **12**, 16625 (2022). https://doi.org/10.1038/s41598-022-20572-2

10 Rothhammer, V. & Quintana, F. J. The aryl hydrocarbon receptor: an environmental sensor integrating immune responses in health and disease. *Nature Reviews Immunology* **19**, 184-197 (2019). https://doi.org/10.1038/s41577-019-0125-8

11 Dong, F. & Perdew, G. H. The aryl hydrocarbon receptor as a mediator of host-microbiota interplay. *Gut Microbes* **12**, 1859812 (2020). https://doi.org/10.1080/19490976.2020.1859812

12 Gutiérrez-Vázquez, C. & Quintana, F. J. Regulation of the Immune Response by the Aryl Hydrocarbon Receptor. *Immunity* **48**, 19-33 (2018). https://doi.org/10.1016/j.immuni.2017.12.012

13 Anandakumar, H. *et al.* Segmental patterning of microbiota and immune cells in the murine intestinal tract. *Gut microbes* **16**, 2398126 (2024). https://doi.org/10.1080/19490976.2024.2398126

14 Voroneanu, L. *et al.* Gut Microbiota in Chronic Kidney Disease: From Composition to Modulation towards Better Outcomes-A Systematic Review. *J Clin Med* **12** (2023). https://doi.org/10.3390/jcm12051948

15 Chaves, L. D. *et al.* Chronic kidney disease, uremic milieu, and its effects on gut bacterial microbiota dysbiosis. *Am J Physiol Renal Physiol* **315**, F487-f502 (2018). https://doi.org/10.1152/ajprenal.00092.2018

16 Bloom, P. P. *et al.* Microbiota and kidney disease: the road ahead. *Nature Reviews Nephrology* **21**, 702-716 (2025). https://doi.org/10.1038/s41581-025-00988-5

17 Chen, T. K., Knicely, D. H. & Grams, M. E. Chronic Kidney Disease Diagnosis and Management: A Review. *Jama* **322**, 1294-1304 (2019). https://doi.org/10.1001/jama.2019.14745

18 Patel, N., Yaqoob, M. M. & Aksentijevic, D. Cardiac metabolic remodelling in chronic kidney disease. *Nature Reviews Nephrology* **18**, 524-537 (2022). https://doi.org/10.1038/s41581-022-00576-x

19 Kaptoge, S. *et al.* C-reactive protein concentration and risk of coronary heart disease, stroke, and mortality: an individual participant meta-analysis. *Lancet* **375**, 132-140 (2010). https://doi.org/10.1016/s0140-6736(09)61717-7

20 Marques, F. Z., Mackay, C. R. & Kaye, D. M. Beyond gut feelings: how the gut microbiota regulates blood pressure. *Nature Reviews Cardiology* **15**, 20-32 (2018). https://doi.org/10.1038/nrcardio.2017.120

21 Avery, E. G. *et al.* Quantifying the impact of gut microbiota on inflammation and hypertensive organ damage. *Cardiovasc Res* **119**, 1441-1452 (2023). https://doi.org/10.1093/cvr/cvac121

22 Yang, B. H. *et al.* Foxp3+ T cells expressing RORγt represent a stable regulatory T-cell effector lineage with enhanced suppressive capacity during intestinal inflammation. *Mucosal Immunology* **9**, 444-457 (2016). https://doi.org/10.1038/mi.2015.74

23 Blatner, N. R. *et al.* Expression of RORγt marks a pathogenic regulatory T cell subset in human colon cancer. *Sci Transl Med* **4**, 164ra159 (2012). https://doi.org/10.1126/scitranslmed.3004566

24 Rothhammer, V. & Quintana, F. J. The aryl hydrocarbon receptor: an environmental sensor integrating immune responses in health and disease. *Nature reviews. Immunology* **19**, 184-197 (2019). https://doi.org/10.1038/s41577-019-0125-8

25 Quintana, F. J. *et al.* Control of T(reg) and T(H)17 cell differentiation by the aryl hydrocarbon receptor. *Nature* **453**, 65-71 (2008). https://doi.org/10.1038/nature06880

26 Veldhoen, M. *et al.* The aryl hydrocarbon receptor links TH17-cell-mediated autoimmunity to environmental toxins. *Nature* **453**, 106-109 (2008). https://doi.org/10.1038/nature06881

27 Delgobo, M. *et al.* Myocardial Milieu Favors Local Differentiation of Regulatory T Cells. *Circulation research* **132**, 565-582 (2023). https://doi.org/10.1161/CIRCRESAHA.122.322183

28 Hwang, S. J. *et al.* Indoxyl 3-sulfate stimulates Th17 differentiation enhancing phosphorylation of c-Src and STAT3 to worsen experimental autoimmune encephalomyelitis. *Toxicol Lett* **220**, 109-117 (2013). https://doi.org/10.1016/j.toxlet.2013.04.016

29 Schiattarella, G. G. *et al.* Nitrosative stress drives heart failure with preserved ejection fraction. *Nature* **568**, 351-356 (2019). https://doi.org/10.1038/s41586-019-1100-z

30 Bansal, N., Zelnick, L. R., Scherzer, R., Estrella, M. & Shlipak, M. G. Risk Factors and Outcomes Associated With Heart Failure With Preserved and Reduced Ejection Fraction in People With Chronic Kidney Disease. *Circulation. Heart failure* **17**, e011173 (2024). https://doi.org/10.1161/CIRCHEARTFAILURE.123.011173

31 Meijers, B. K. *et al.* p-Cresyl sulfate and indoxyl sulfate in hemodialysis patients. *Clin J Am Soc Nephrol* **4**, 1932-1938 (2009). https://doi.org/10.2215/cjn.02940509

1311 32 Kaesler, N. *et al.* Mapping cardiac remodeling in chronic kidney disease. *Sci Adv* **9**,
1312 eadj4846 (2023). https://doi.org/10.1126/sciadv.adj4846
1313 33 Naba, A. *et al.* The matrisome: in silico definition and in vivo characterization by
1314 proteomics of normal and tumor extracellular matrices. *Mol Cell Proteomics* **11**,
1315 M111.014647 (2012). https://doi.org/10.1074/mcp.M111.014647
1316 34 Patrick, R. *et al.* Integration mapping of cardiac fibroblast single-cell transcriptomes
1317 elucidates cellular principles of fibrosis in diverse pathologies. *Science Advances* **10**,
1318 eadk8501 (2024). https://doi.org/10.1126/sciadv.adk8501
1319 35 Barallobre-Barreiro, J. *et al.* Glycoproteomics Reveals Decorin Peptides With Anti-
1320 Myostatin Activity in Human Atrial Fibrillation. *Circulation* **134**, 817-832 (2016).
1321 https://doi.org/10.1161/CIRCULATIONAHA.115.016423
1322 36 Kober, C. *et al.* Targeting the aryl hydrocarbon receptor (AhR) with BAY 2416964: a
1323 selective small molecule inhibitor for cancer immunotherapy. *J Immunother Cancer*
1324 **11** (2023). https://doi.org/10.1136/jitc-2023-007495
1325 37 Kuppe, C. *et al.* Decoding myofibroblast origins in human kidney fibrosis. *Nature* **589**,
1326 281-286 (2021). https://doi.org/10.1038/s41586-020-2941-1
1327 38 Batra, G. *et al.* Interleukin 6 and Cardiovascular Outcomes in Patients With Chronic
1328 Kidney Disease and Chronic Coronary Syndrome. *JAMA Cardiol* **6**, 1440-1445 (2021).
1329 https://doi.org/10.1001/jamacardio.2021.3079
1330 39 Tonelli, M., Karumanchi, S. A. & Thadhani, R. Epidemiology and Mechanisms of
1331 Uremia-Related Cardiovascular Disease. *Circulation* **133**, 518-536 (2016).
1332 https://doi.org/doi:10.1161/CIRCULATIONAHA.115.018713
1333 40 Hayer, M. K. *et al.* Defining Myocardial Abnormalities Across the Stages of Chronic
1334 Kidney Disease: A Cardiac Magnetic Resonance Imaging Study. *JACC Cardiovasc*
1335 *Imaging* **13**, 2357-2367 (2020). https://doi.org/10.1016/j.jcmg.2020.04.021
1336 41 Bansal, N. *et al.* Burden and Outcomes of Heart Failure Hospitalizations in Adults
1337 With Chronic Kidney Disease. *Journal of the American College of Cardiology* **73**, 2691-
1338 2700 (2019). https://doi.org/10.1016/j.jacc.2019.02.071
1339 42 Schulman, G. *et al.* Randomized Placebo-Controlled EPPIC Trials of AST-120 in CKD.
1340 *Journal of the American Society of Nephrology : JASN* **26**, 1732-1746 (2015).
1341 https://doi.org/10.1681/ASN.2014010042
1342 43 Holle, J. *et al.* Inflammation in Children with CKD Linked to Gut Dysbiosis and
1343 Metabolite Imbalance. *J Am Soc Nephrol* **33**, 2259-2275 (2022).
1344 https://doi.org/10.1681/asn.2022030378
1345 44 Collett, J. A. *et al.* IL-17A Levels and Progression of Kidney Disease Following
1346 Hospitalization with and without Acute Kidney Injury. *Kidney360* **5**, 1623-1632
1347 (2024). https://doi.org/10.34067/kid.0000000000000559
1348 45 Kimura, A., Naka, T., Nohara, K., Fujii-Kuriyama, Y. & Kishimoto, T. Aryl hydrocarbon
1349 receptor regulates Stat1 activation and participates in the development of Th17
1350 cells. *Proceedings of the National Academy of Sciences* **105**, 9721-9726 (2008).
1351 https://doi.org/doi:10.1073/pnas.0804231105
1352 46 Schroeder, J. C. *et al.* The uremic toxin 3-indoxyl sulfate is a potent endogenous
1353 agonist for the human aryl hydrocarbon receptor. *Biochemistry* **49**, 393-400 (2010).
1354 https://doi.org/10.1021/bi901786x
1355 47 Kaminski, T. W., Pawlak, K., Karbowska, M., Mysliwiec, M. & Pawlak, D. Indoxyl
1356 sulfate - the uremic toxin linking hemostatic system disturbances with the

prevalence of cardiovascular disease in patients with chronic kidney disease. *BMC Nephrol* **18**, 35 (2017). https://doi.org/10.1186/s12882-017-0457-1

48 Lochner, M. *et al.* In vivo equilibrium of proinflammatory IL-17+ and regulatory IL-10+ Foxp3+ RORgamma t+ T cells. *The Journal of experimental medicine* **205**, 1381-1393 (2008). https://doi.org/10.1084/jem.20080034

49 Kim, M. J. *et al.* Deletion of PD-1 destabilizes the lineage identity and metabolic fitness of tumor-infiltrating regulatory T cells. *Nature immunology* **24**, 148-161 (2023). https://doi.org/10.1038/s41590-022-01373-1

50 Cortes, J. R. *et al.* Maintenance of immune tolerance by Foxp3+ regulatory T cells requires CD69 expression. *Journal of autoimmunity* **55**, 51-62 (2014). https://doi.org/10.1016/j.jaut.2014.05.007

51 Ichikawa, T. *et al.* CD103(hi) T(reg) cells constrain lung fibrosis induced by CD103(lo) tissue-resident pathogenic CD4 T cells. *Nature immunology* **20**, 1469-1480 (2019). https://doi.org/10.1038/s41590-019-0494-y

52 Mantovani, A., Cassatella, M. A., Costantini, C. & Jaillon, S. Neutrophils in the activation and regulation of innate and adaptive immunity. *Nature Reviews Immunology* **11**, 519-531 (2011). https://doi.org/10.1038/nri3024

53 Stark, M. A. *et al.* Phagocytosis of Apoptotic Neutrophils Regulates Granulopoiesis via IL-23 and IL-17. *Immunity* **22**, 285-294 (2005). https://doi.org/https://doi.org/10.1016/j.immuni.2005.01.011

54 Wilson, A. S. *et al.* Neutrophil extracellular traps and their histones promote Th17 cell differentiation directly via TLR2. *Nature Communications* **13**, 528 (2022). https://doi.org/10.1038/s41467-022-28172-4

55 Valente, A. J. *et al.* Interleukin-17A stimulates cardiac fibroblast proliferation and migration via negative regulation of the dual-specificity phosphatase MKP-1/DUSP-1. *Cellular Signalling* **24**, 560-568 (2012). https://doi.org/https://doi.org/10.1016/j.cellsig.2011.10.010

56 Wu, L. *et al.* Cardiac fibroblasts mediate IL-17A-driven inflammatory dilated cardiomyopathy. *The Journal of experimental medicine* **211**, 1449-1464 (2014). https://doi.org/10.1084/jem.20132126

57 Träger, C. *et al.* A probiotic approach identifies a Treg-centred immunoregulation via modulation of gut microbiota metabolites in people with multiple sclerosis and healthy individuals. *EBioMedicine* **116**, 105743 (2025). https://doi.org/10.1016/j.ebiom.2025.105743

58 Thiele, A. *et al.* Pharmacological inhibition of adipose tissue adipose triglyceride lipase by Atglistatin prevents catecholamine-induced myocardial damage. *Cardiovasc Res* **118**, 2488-2505 (2022). https://doi.org/10.1093/cvr/cvab182

59 Beyhoff, N. *et al.* Application of Speckle-Tracking Echocardiography in an Experimental Model of Isolated Subendocardial Damage. *J Am Soc Echocardiogr* **30**, 1239-1250.e1232 (2017). https://doi.org/10.1016/j.echo.2017.08.006

60 Sadik, A. *et al.* IL4I1 Is a Metabolic Immune Checkpoint that Activates the AHR and Promotes Tumor Progression. *Cell* **182**, 1252-1270.e1234 (2020). https://doi.org/10.1016/j.cell.2020.07.038

61 Finak, G. *et al.* MAST: a flexible statistical framework for assessing transcriptional changes and characterizing heterogeneity in single-cell RNA sequencing data. *Genome Biology* **16**, 278 (2015). https://doi.org/10.1186/s13059-015-0844-5

1403 62 Cui, A. *et al.* Dictionary of immune responses to cytokines at single-cell resolution.
1404 *Nature* **625**, 377-384 (2024). https://doi.org/10.1038/s41586-023-06816-9
1405 63 Versnjak, J. *et al.* Deep phenotyping of heart failure with preserved ejection fraction
1406 through multi-omics integration. *Eur J Heart Fail* (2025).
1407 https://doi.org/10.1002/ejhf.70041

1408

1409 **Figure Legends**

1410 **Figure 1. Depletion of microbiome-derived metabolites attenuates cardiac**
1411 **remodeling in mice with impaired kidney function. (a)** 129/Sv mice were
1412 randomized to receive a broad-spectrum, oral antibiotic cocktail (Abx) or control
1413 drinking water. After one week, mice underwent two-stage subtotal nephrectomy
1414 (STNx) or sham surgery. **(b)** Representative ^{1}H-NMR plasma spectra 13 weeks after
1415 surgery and **(c)** determination of summed-up peak areas within the aromatic region,
1416 normalized to the respective sham group. **(d)** Heatmap of plasma metabolites
1417 quantified by liquid chromatography-mass spectrometry (LC-MS). **(e)** Plasma
1418 concentrations of sulfated microbiome-derived metabolites quantified by LC-MS.
1419 Transdermal glomerular filtration rate (GFR) normalized measured **(f)** longitudinally
1420 and **(g)** at endpoint. **(h)** Heart weight normalized to tibia length at the endpoint. **(i)**
1421 Representative echocardiographic images at the endpoint. **(j)** Left ventricular posterior
1422 wall thickness at end-diastole (LVPWd). **(k)** Longitudinal changes in normalized left
1423 ventricular (LV) mass. **(l)** Ejection fraction (EF), **(m)** E/e′ ratio, **(n)** global longitudinal
1424 strain (GLS) at the endpoint. **(o)** Histological assessment of left ventricular fibrosis by
1425 Sirius Red staining (scale bars: upper, 1 mm; lower, 100 µm) and **(p)** quantification of
1426 fibrotic area. **(q)** Quantification of leukocytes in the heart at the endpoint by flow
1427 cytometry. **(r)** Plasma C-reactive protein (CRP) levels at the endpoint. **(s)**
1428 Radiotelemetric blood pressure (BP) measurement. **(t)** Representative average
1429 systolic BP (SBP) plots at baseline (week 0) and week 12, and **(u)** quantification. **(v)**
1430 Acetylcholine (ACh)-induced endothelial-dependent vasorelaxation of mesenteric
1431 arteries assessed by wire myography, and **(w)** corresponding EC_{50} values. Symbols
1432 in **(f)** and **(k)** indicate the following comparisons: Sham vs. STNx (‡), Sham Abx vs.
1433 STNx Abx (#), and STNx vs. STNx Abx (*). Data are shown as mean ± SEM. Each dot
1434 represents one mouse. Statistical analyses were performed using one-way ANOVA or
1435 Kruskal-Wallis test followed by Tukey's or Dunn's *post hoc* correction, as appropriate,
1436 unless otherwise indicated. Mann Whitney U-tests with false discovery rate correction
1437 according to Benjamini-Hochberg were used for metabolomics data. Two-group
1438 comparisons for the aromatic NMR region **(c)** and EC_{50} values **(w)** were performed
1439 using unpaired two-tailed Student's t test. Two-group comparisons of systolic blood
1440 pressure in **(u)** were assessed by Mann-Whitney U test.

1441

1442 **Figure 2. Kidney disease induces microbiota-dependent Th17-driven systemic**
1443 **and cardiac inflammation.** Immune cells were isolated from spleens and analyzed
1444 by flow cytometry. **(a)** Abundance of neutrophils ($CD45^+$ $CD3^-$ $NK1.1^-$ $CD11b^+$ $Ly6G^+$)
1445 among $CD45^+$ cells. **(b)** Ratio of T helper (T_H, $CD45^+$ $CD3^+$ $TCR\gamma\delta^-$ $CD4^+$ $CD8^-$) to
1446 cytotoxic T cells (T_C, $CD45^+$ $CD3^+$ $TCR\gamma\delta^-$ $CD4^+$ $CD8^-$). **(c)** UMAP projection of splenic
1447 T cell populations based on flow cytometry. **(d)** Frequencies of effector memory (EM,
1448 $CD44^+$ $CD62L^-$) conventional T cells (T_{conv}, $FoxP3^-$ T_H). **(e)** Frequencies of EM
1449 regulatory T cells (T_{reg}, $FoxP3^+$ T_H). **(f)** Frequencies of $ROR\gamma t^+$ T_{conv}. **(g)** Changes in
1450 $ROR\gamma t^+$ T_{conv} abundance between experimental groups
1451 (* p-adj. < 0.1). **(h)** Frequencies of $ROR\gamma t^+$ T_{reg}. **(i)** Longitudinal frequencies of $ROR\gamma t^+$
1452 T_{conv} (left) and T_{reg} (right). **(j)** Aryl hydrocarbon receptor (AhR) activation of plasma in
1453 reporter cell line. **(k)** *Cyp1a1* expression in splenocytes. **(l)** Representative flow
1454 cytometric plots of cardiac $ROR\gamma t^+$ T_{reg} ($T_{reg}17$) and **(m)** quantification. **(n)** Overlap of
1455 differentially expressed genes (DEG) in cardiac bulk mRNA-sequencing between the
1456 two indicated comparisons. **(o)** Significantly enriched biological pathways in the
1457 cardiac transcriptome. **(p)** Targeted gene ontology (GO) and pathway analysis of IL-
1458 17A-related differentially enriched gene sets. Data are shown as mean ± SEM. Each
1459 dot represents one mouse. Statistical analyses were performed using one-way
1460 ANOVA or Kruskal-Wallis test followed by Tukey's or Dunn's *post hoc* correction, as
1461 appropriate, unless otherwise indicated. For **(g)**, Benjamini-Hochberg false discovery
1462 rate (FDR) correction was performed. For RNA sequencing, DEG were generated
1463 using the DeSeq2 pipeline with appropriate FDR correction. Gene set enrichment
1464 analyses were performed using Fisher's exact test followed by FDR correction.

1465

1466 **Figure 3. Indoxyl sulfate induces inflammation and cardiac fibrosis independent**
1467 **of kidney function. (a, b)** *In vitro* T_H17 differentiation of naïve T helper cells from
1468 129/Sv mice in the presence and absence of indoxyl sulfate (IxS). Two biological
1469 replicates, three technical replicates each. **(c)** Heart failure with preserved ejection
1470 fraction was induced in 129/Sv mice using high-fat diet (HFD) and L-NAME in the
1471 drinking water for 15 weeks. Mice received either IxS or potassium chloride (KCl,
1472 control) in the drinking water throughout the experiment. **(d)** Plasma IxS measured by
1473 liquid chromatography-mass spectrometry (LC-MS). **(e)** Plasma cystatin C levels. (f)
1474 *Cyp1a1* expression in spleen. Flow cytometric quantification of IL17A in splenic **(g)**

1475 T_{conv} ($CD45^+$ $CD3^+$ TCRγδ$^-$ $CD4^+$ $CD8^-$ $FoxP3^-$) and **(h)** T_{reg} ($CD45^+$ $CD3^+$ TCRγδ$^-$
1476 $CD4^+$ $CD8^-$ $FoxP3^+$). **(i)** Heart weight normalized to tibia length. **(j)** Cardiac interstitial
1477 fibrosis, assessed by histological staining for collagen type I (COL-1) and fibronectin
1478 (FN-1) (scale bar: 100 μm), with quantification of **(k)** FN-1 and **(l)** COL-1. Data are
1479 shown as mean ± SEM. Each dot represents one mouse. Statistical analyses were
1480 performed using one-tailed Student's t test or Mann-Whitney U-test, as appropriate.
1481 **(b)** Statistical analysis was performed using linear regression.

1482

1483 **Figure 4. IL-17A-signaling in IxS-primed cardiac fibroblasts promotes**
1484 **extracellular matrix production.** Cardiac *Il17ra* expression in **(a)** 129/Sv mice
1485 subjected to subtotal nephrectomy (STNx) or sham operation and treated with either
1486 an antibiotic cocktail (Abx) or control drinking water, and in **(b)** 129/Sv mice subjected
1487 to high-fat diet (HFD) plus L-NAME and indoxyl sulfate (IxS) or potassium chloride
1488 (KCl, control) in the drinking water. Re-analysis of previously published cardiac single
1489 nuclei (sn) RNA-sequencing data (Kaesler *et al.*) from STNx mice shows **(c)** highest
1490 *Il17ra* expression in fibroblasts and **(d)** higher extracellular matrix (ECM) gene set
1491 score in *Il17ra* expressing cardiac fibroblasts. **(e)** Enrichment analysis for known
1492 cardiac fibroblasts subtypes within differentially expressed genes. **(f)** Cardiac
1493 fibroblasts were isolated from C57BL/6J mice for *ex vivo* treatment with IxS and IL-
1494 17A. Purity validation **(g)** by histology using platelet-derived growth factor receptor
1495 alpha (PDGFRA) and vimentin (VIM) (scale bar: 100 μm), and **(h)** by flow cytometry
1496 showing $CD45^-$ $CD31^-$ $PDGFRA^+$ fibroblasts. **(i)** *Il17ra* expression following *in vitro*
1497 incubation with IxS. Isolated fibroblasts were incubated with 100μM IxS, 1ng/mL IL-
1498 17A, or both and expression of **(j)** *Col1a1*, **(k)** *Col1a2*, **(l)** *Acta2*, **(m)** *Abi3bp* were
1499 quantified. **(n)** Histological confirmation of IL-17RA expression in cardiac fibroblasts
1500 (scale bar: 100 μm). **(a, b)** Data are shown as mean ± SEM. Each dot represents one
1501 mouse. **(i-m)** Data are combined from four biological replicates, with three technical
1502 replicates each. Statistical analyses were performed using one-way ANOVA or
1503 Kruskal-Wallis test followed by Tukey's or Dunn's *post hoc* correction, as appropriate.
1504 **(b)** Statistical analysis was performed using one-tailed Student's t test. **(d)** Comparison
1505 by two-sided Mann-Whitney U-test.

1506

1507 **Figure 5. Pharmacological blockade of the AhR ameliorates inflammation and**
1508 **cardiac remodeling in kidney disease. (a)** *Ex vivo* aryl hydrocarbon receptor (AhR)
1509 inhibition in immune cells from 129/Sv mice with BAY 2416964 (AhRi). **(b)** AhRi blocks
1510 indoxyl sulfate (IxS)-induced *Cyp1a1* gene expression in splenocytes. **(c)** AhRi
1511 suppresses IxS-enhanced TH17 differentiation of naïve T cells. **(d)** 129/Sv mice
1512 underwent two stage subtotal nephrectomy (STNx) or sham surgery. Two weeks after
1513 completion of surgery, STNx mice were randomized to AhRi or vehicle (VEH)
1514 treatment based on plasma cystatin C. **(e)** Survival analysis according to pre-specified
1515 humane endpoints. **(f)** Plasma C-reactive protein (CRP) levels. **(g)** *Cyp1a1* expression
1516 in splenocytes. RORγt in splenic **(h)** T_{conv} ($CD45^+$ $CD3^+$ $TCR\gamma\delta^-$ $CD4^+$ $CD8^-$ $FoxP3^-$)
1517 and **(i)** T_{reg} ($CD45^+$ $CD3^+$ $TCR\gamma\delta^-$ $CD4^+$ $CD8^-$ $FoxP3^+$) by flow cytometry. **(j)** Left
1518 ventricular (LV) mass normalized to tibia length, **(i)** E/e' ratio and **(l)** global longitudinal
1519 strain (GLS) from endpoint echocardiography. **(m)** Cardiac fibrosis assessed by Sirius
1520 Red staining (scale bar top: 1mm, bottom: 100µm). **(n)** Quantification of Sirius Red-
1521 positive interstitial fibrosis. **(o)** Cardiac *Il17ra* expression. **(p)** Enriched biological
1522 pathways among differentially expressed genes significant in STNx rescued by AhRi.
1523 **(q)** Targeted gene ontology (GO) analysis of IL-17A-related differentially expressed
1524 gene sets. **(b-c)** Data are combined from three technical replicates. **(c)** Data were
1525 analyzed by nonlinear sigmoidal regression. **(e-o)** Data are shown as mean ± SEM.
1526 Each dot represents one mouse. Statistical analyses were performed using one-way
1527 ANOVA or Kruskal-Wallis test followed by Tukey's or Dunn's *post hoc* correction, as
1528 appropriate, unless otherwise indicated. Gene set enrichment analyses were
1529 performed using Fisher's exact test.

1530

1531 **Figure 6. Validation of the pro-fibrotic AhR-IL-17A axis in patients with chronic**
1532 **kidney disease. (a)** Activation of aryl hydrocarbon receptor (AhR) in HT29-Lucia AhR
1533 reporter cells with 100µM indoxyl sulfate (IxS) is blockable by the AhR inhibitor BAY
1534 2416964 (AhRi). **(b)** Serum was obtained from healthy controls (HC) or patients with
1535 chronic kidney disease treated with hemodialysis (HD) for *in vitro* testing on AhR
1536 reporter and naïve T cells. **(c)** Activation of the AhR in response to HC or HD serum
1537 in the presence or absence of AhRi. **(d)** *In vitro* T_H17 differentiation of naïve T cells
1538 from healthy volunteers in the presence of HC and HD serum. **(e)** Plasma IL-17A
1539 derived from OLINK Explore HT in the UK Biobank (UKBB) stratified by estimated

1540 glomerular filtration rate (eGFR) and albuminuria in patients with available data.
1541 Statistical comparisons are made between the reference cell (G1, A1) and each
1542 corresponding cell. Adjusted p-values indicate significance as follows: *** < 0.001,
1543 ** < 0.01, * < 0.05. **(f)** Plasma IL-17A in patients with CKD defined by an eGFR < 60
1544 mL/min/1.73 m². with and without heart failure with persevered ejection fraction
1545 (HFpEF). **(g)** Kaplan-Meier survival curves for all-cause mortality stratified by IL-17A
1546 levels (<25th, 25th -75th, >75th percentile) among participants with eGFR < 60
1547 mL/min/1.73 m². **(h)** Corresponding hazard ratios and 95% confidence intervals from
1548 a Cox proportional hazards model for all-cause mortality. Model 1 only IL-17A. Model
1549 2 additionally adjusted for age, sex, and eGFR. Model 3 further adjusted for
1550 hypertension, diabetes, pack years, BMI, and NT-proBNP. **(i)** Human primary cardiac
1551 fibroblasts were incubated *in vitro* with HC and HD serum in addition of anti-IL-17A
1552 (Secukinumab, αIL17A) or AhRi and analyzed for **(j)** *IL17RA*, **(k)** *COL1A1*, **(l)** *COL1A2*,
1553 and **(m)** *ACTA2* expression. **(a, c)** Data are combined from three biological replicates,
1554 with three technical replicates each and **(h-k)** data combined from two primary cell
1555 lines from different donors treated with HC serum (n = 4 donors) or HD serum (n = 9
1556 donors) in triplicates. Statistical analyses were performed using one-way ANOVA or
1557 Kruskal-Wallis test followed by Tukey's or Dunn's *post hoc* correction, as appropriate.

Figure 1

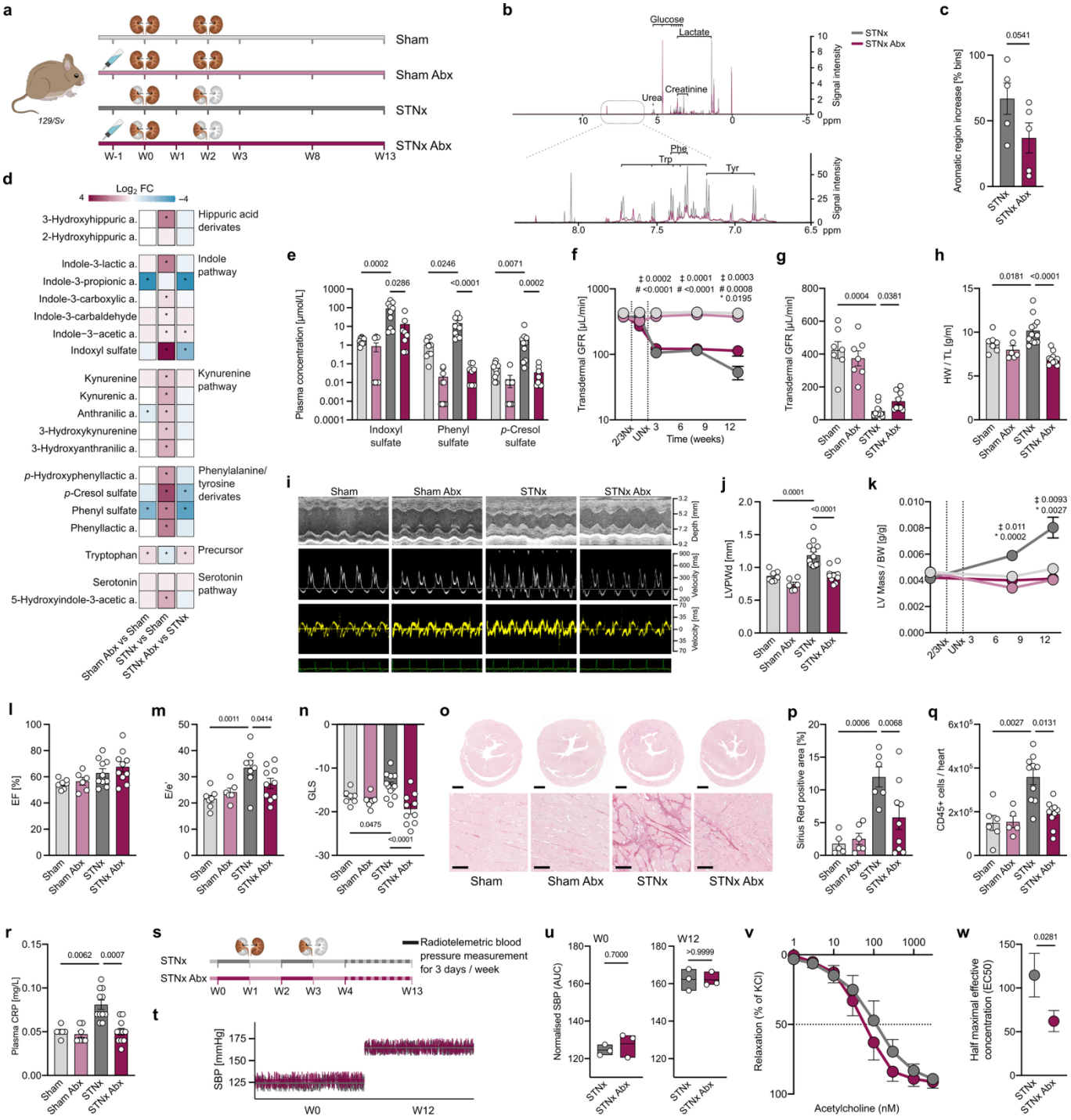
a
Sham
Sham Abx
STNx
STNx Abx
129/Sv
W-1 W0 W1 W2 W3 W8 W13
b
Glucose
Lactate
Creatinine
Urea
Phe
Trp
Tyr
STNx
STNx Abx
Signal intensity
ppm
c
Aromatic region increase [% bins]
0.0541
d
Log2 FC
3-Hydroxyhippuric a.
2-Hydroxyhippuric a.
Hippuric acid derivates
Indole-3-lactic a.
Indole-3-propionic a.
Indole-3-carboxylic a.
Indole-3-carbaldehyde
Indole−3−acetic a.
Indoxyl sulfate
Indole pathway
Kynurenine
Kynurenic a.
Anthranilic a.
3-Hydroxykynurenine
3-Hydroxyanthranilic a.
Kynurenine pathway
p-Hydroxyphenyllactic a.
p-Cresol sulfate
Phenyl sulfate
Phenyllactic a.
Phenylalanine/ tyrosine derivates
Tryptophan
Precursor
Serotonin
5-Hydroxyindole-3-acetic a.
Serotonin pathway
Sham Abx vs Sham
STNx vs Sham
STNx Abx vs STNx
e
Plasma concentration [µmol/L]
Indoxyl sulfate
Phenyl sulfate
p-Cresol sulfate
f
Transdermal GFR [µL/min]
Time (weeks)
2/3Nx
UNx
g
Transdermal GFR [µL/min]
h
HW / TL [g/m]
i
Sham
Sham Abx
STNx
STNx Abx
Depth [mm]
Velocity [ms]
j
LVPWd [mm]
k
LV Mass / BW [g/g]
l
EF [%]
m
E/e'
n
GLS
o
Sham
Sham Abx
STNx
STNx Abx
p
Sirius Red positive area [%]
q
CD45+ cells / heart
r
Plasma CRP [mg/L]
s
STNx
STNx Abx
Radiotelemetric blood pressure measurement for 3 days / week
W0 W1 W2 W3 W4 W13
t
SBP [mmHg]
W0
W12
u
W0
W12
Normalised SBP (AUC)
v
Relaxation (% of KCl)
Acetylcholine (nM)
w
Half maximal effective concentration (EC50)

Figure 2

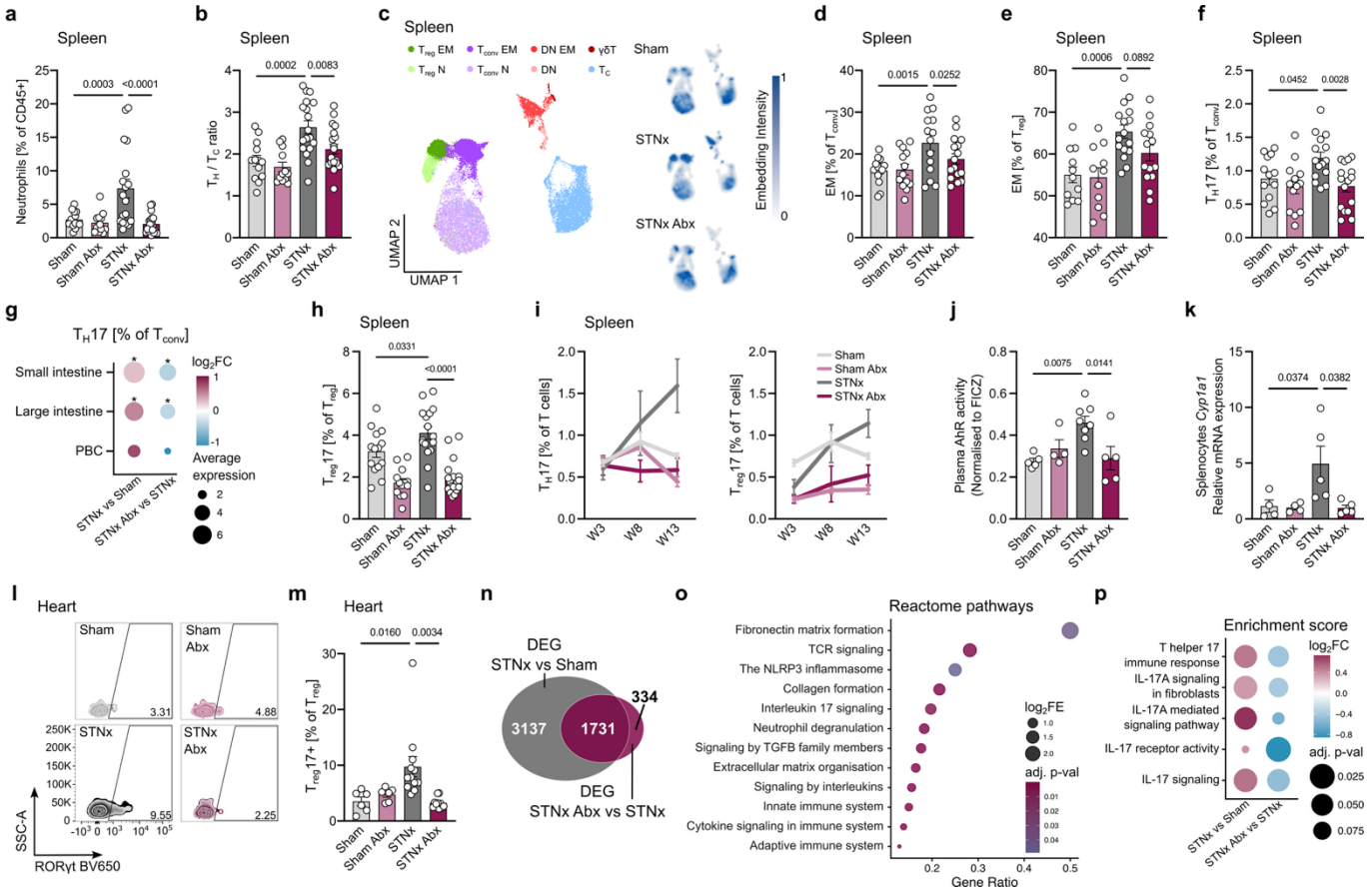
a
Spleen
Neutrophils [% of CD45+]
0.0003
<0.0001
Sham
Sham Abx
STNx
STNx Abx
b
Spleen
T_H / T_C ratio
0.0002
0.0083
c
Spleen
T_{reg} EM
T_{conv} EM
DN EM
γδT
T_{reg} N
T_{conv} N
DN
T_C
UMAP 1
UMAP 2
Sham
STNx
STNx Abx
Embedding Intensity
d
Spleen
EM [% of T_{conv}]
0.0015
0.0252
e
Spleen
EM [% of T_{reg}]
0.0006
0.0892
f
Spleen
T_H17 [% of T_{conv}]
0.0452
0.0028
g
T_H17 [% of T_{conv}]
Small intestine
Large intestine
PBC
STNx vs Sham
STNx Abx vs STNx
log_2FC
Average expression
h
Spleen
$T_{reg}17$ [% of T_{reg}]
0.0331
<0.0001
i
Spleen
T_H17 [% of T cells]
$T_{reg}17$ [% of T cells]
W3
W8
W13
Sham
Sham Abx
STNx
STNx Abx
j
Plasma AhR activity (Normalised to FICZ)
0.0075
0.0141
k
Splenocytes *Cyp1a1* Relative mRNA expression
0.0374
0.0382
l
Heart
Sham
Sham Abx
STNx
STNx Abx
3.31
4.88
9.55
2.25
SSC-A
RORγt BV650
m
Heart
$T_{reg}17$+ [% of T_{reg}]
0.0160
0.0034
n
DEG
STNx vs Sham
3137
1731
334
DEG
STNx Abx vs STNx
o
Reactome pathways
Fibronectin matrix formation
TCR signaling
The NLRP3 inflammasome
Collagen formation
Interleukin 17 signaling
Neutrophil degranulation
Signaling by TGFB family members
Extracellular matrix organisation
Signaling by interleukins
Innate immune system
Cytokine signaling in immune system
Adaptive immune system
Gene Ratio
log_2FE
adj. p-val
p
Enrichment score
T helper 17 immune response
IL-17A signaling in fibroblasts
IL-17A mediated signaling pathway
IL-17 receptor activity
IL-17 signaling
STNx vs Sham
STNx Abx vs STNx
log_2FC
adj. p-val

Figure 3

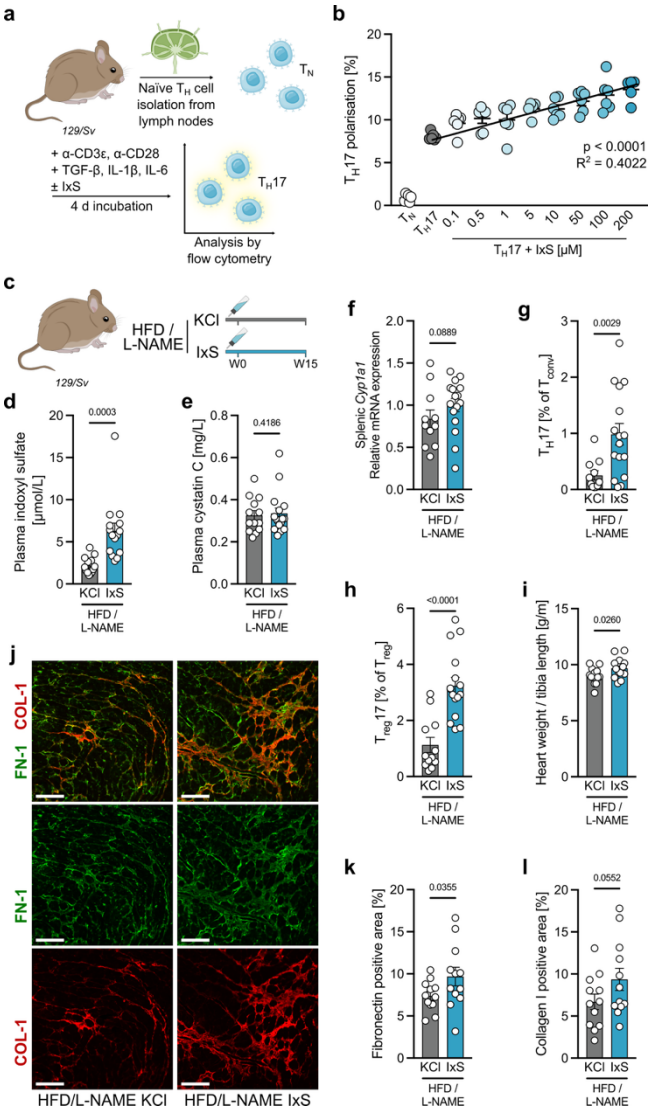
a
129/Sv
Naïve T_H cell isolation from lymph nodes
T_N
+ α-CD3ε, α-CD28
+ TGF-β, IL-1β, IL-6
± IxS
4 d incubation
T_H17
Analysis by flow cytometry
b
T_H17 polarisation [%]
p < 0.0001
R^2 = 0.4022
T_H17 + IxS [μM]
c
HFD / L-NAME
KCl
IxS
W0
W15
d
Plasma indoxyl sulfate [μmol/L]
0.0003
e
Plasma cystatin C [mg/L]
0.4186
f
Splenic Cyp1a1 Relative mRNA expression
0.0889
g
T_H17 [% of T_{conv}]
0.0029
h
$T_{reg}17$ [% of T_{reg}]
<0.0001
i
Heart weight / tibia length [g/m]
0.0260
j
COL-1
FN-1
FN-1
COL-1
HFD/L-NAME KCl
HFD/L-NAME IxS
k
Fibronectin positive area [%]
0.0355
l
Collagen I positive area [%]
0.0552

Figure 4

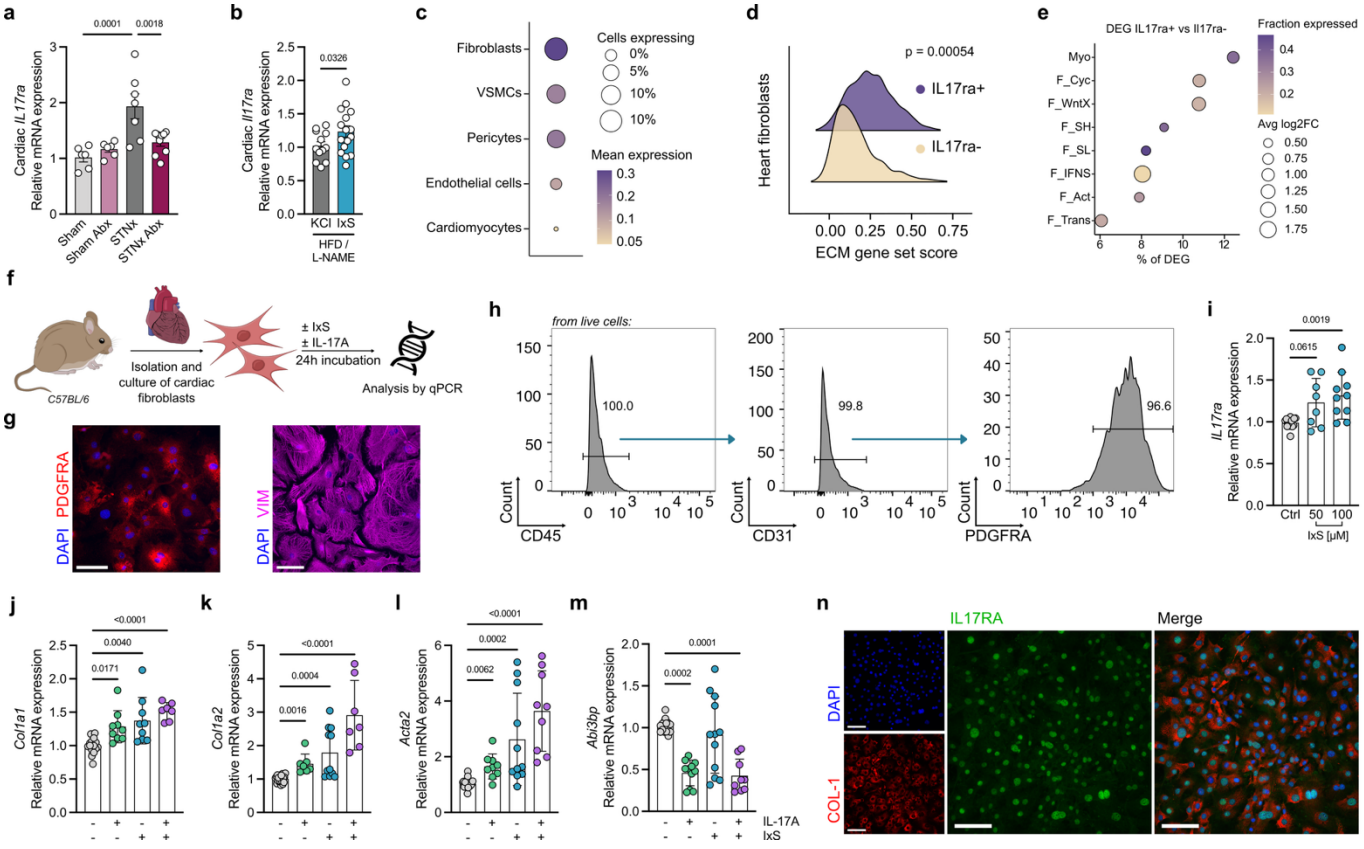
a
Cardiac IL17ra
Relative mRNA expression
0.0001
0.0018
Sham
Sham Abx
STNx
STNx Abx
b
Cardiac Il17ra
Relative mRNA expression
0.0326
KCl
IxS
HFD / L-NAME
c
Fibroblasts
VSMCs
Pericytes
Endothelial cells
Cardiomyocytes
Cells expressing
0%
5%
10%
10%
Mean expression
0.3
0.2
0.1
0.05
d
Heart fibroblasts
p = 0.00054
IL17ra+
IL17ra-
ECM gene set score
e
DEG IL17ra+ vs Il17ra-
Fraction expressed
Avg log2FC
Myo
F_Cyc
F_WntX
F_SH
F_SL
F_IFNS
F_Act
F_Trans
% of DEG
f
C57BL/6
Isolation and culture of cardiac fibroblasts
± IxS
± IL-17A
24h incubation
Analysis by qPCR
g
DAPI PDGFRA
DAPI VIM
h
from live cells:
100.0
99.8
96.6
Count
CD45
CD31
PDGFRA
i
IL17ra
Relative mRNA expression
0.0019
0.0615
Ctrl
50
100
IxS [µM]
j
Col1a1
Relative mRNA expression
<0.0001
0.0040
0.0171
k
Col1a2
Relative mRNA expression
<0.0001
0.0004
0.0016
l
Acta2
Relative mRNA expression
<0.0001
0.0002
0.0062
m
Abi3bp
Relative mRNA expression
0.0001
0.0002
IL-17A
IxS
n
IL17RA
Merge
DAPI
COL-1

Figure 5

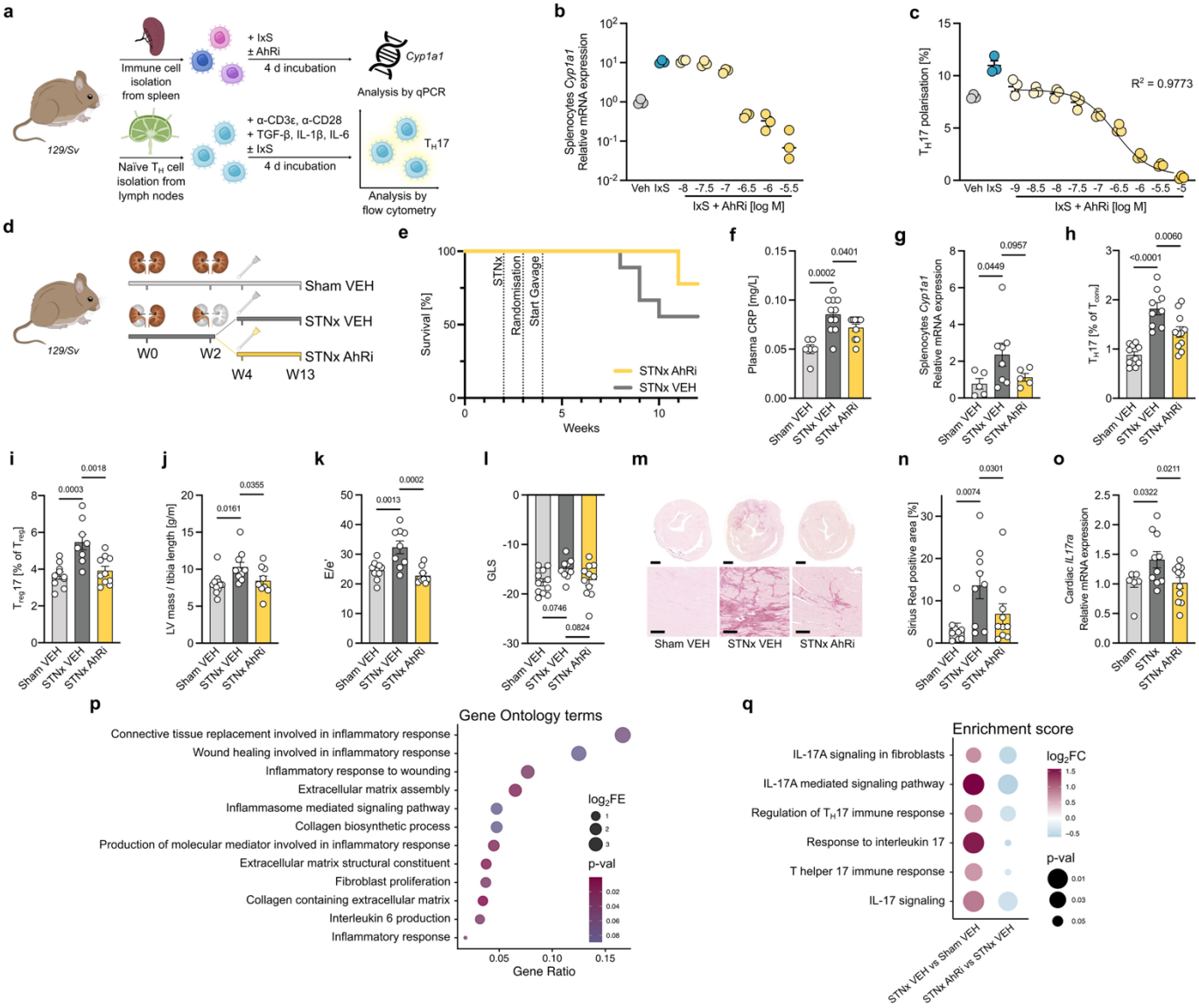
a
129/Sv
Immune cell isolation from spleen
+ IxS
± AhRi
4 d incubation
Cyp1a1
Analysis by qPCR
Naïve T_H cell isolation from lymph nodes
+ α-CD3ε, α-CD28
+ TGF-β, IL-1β, IL-6
± IxS
4 d incubation
T_H17
Analysis by flow cytometry
b
Splenocytes Cyp1a1 Relative mRNA expression
Veh IxS -8 -7.5 -7 -6.5 -6 -5.5
IxS + AhRi [log M]
c
T_H17 polarisation [%]
R^2 = 0.9773
Veh IxS -9 -8.5 -8 -7.5 -7 -6.5 -6 -5.5 -5
IxS + AhRi [log M]
d
129/Sv
Sham VEH
STNx VEH
STNx AhRi
W0
W2
W4
W13
e
Survival [%]
STNx
Randomisation
Start Gavage
STNx AhRi
STNx VEH
Weeks
f
Plasma CRP [mg/L]
0.0002
0.0401
g
Splenocytes Cyp1a1 Relative mRNA expression
0.0449
0.0957
h
T_H17 [% of T_{conv}]
<0.0001
0.0060
i
$T_{reg}17$ [% of T_{reg}]
0.0003
0.0018
j
LV mass / tibia length [g/m]
0.0161
0.0355
k
E/e'
0.0013
0.0002
l
GLS
0.0746
0.0824
m
Sham VEH
STNx VEH
STNx AhRi
n
Sirius Red positive area [%]
0.0074
0.0301
o
Cardiac IL17ra Relative mRNA expression
0.0322
0.0211
Sham VEH
STNx VEH
STNx AhRi
Sham
STNx
p
Gene Ontology terms
Connective tissue replacement involved in inflammatory response
Wound healing involved in inflammatory response
Inflammatory response to wounding
Extracellular matrix assembly
Inflammasome mediated signaling pathway
Collagen biosynthetic process
Production of molecular mediator involved in inflammatory response
Extracellular matrix structural constituent
Fibroblast proliferation
Collagen containing extracellular matrix
Interleukin 6 production
Inflammatory response
log2FE
p-val
Gene Ratio
q
Enrichment score
IL-17A signaling in fibroblasts
IL-17A mediated signaling pathway
Regulation of T_H17 immune response
Response to interleukin 17
T helper 17 immune response
IL-17 signaling
log2FC
p-val
STNx VEH vs Sham VEH
STNx AhRi vs STNx VEH

Figure 6

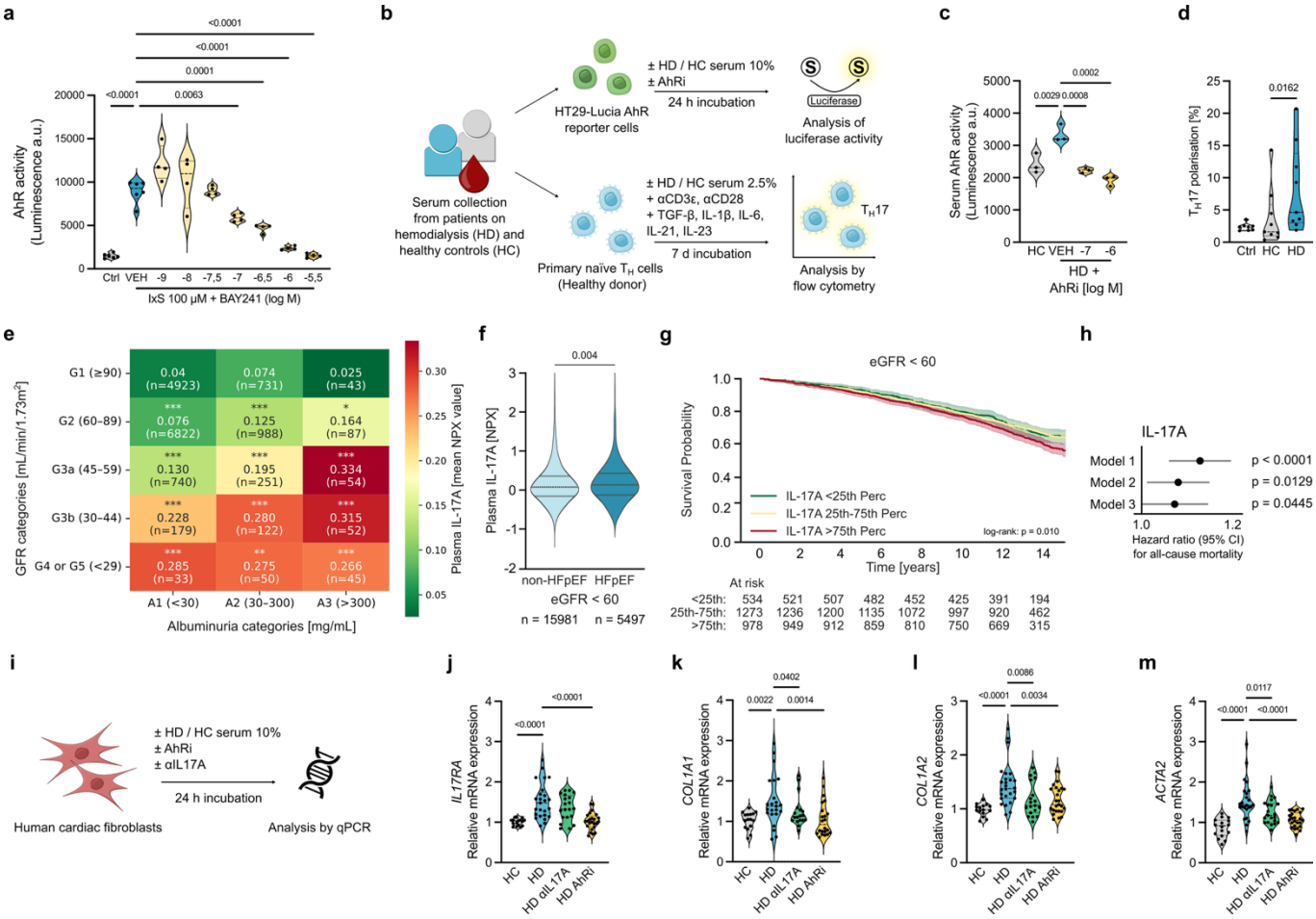
a
AhR activity (Luminescence a.u.)
Ctrl VEH -9 -8 -7,5 -7 -6,5 -6 -5,5
IxS 100 µM + BAY241 (log M)
b
Serum collection from patients on hemodialysis (HD) and healthy controls (HC)
HT29-Lucia AhR reporter cells
± HD / HC serum 10%
± AhRi
24 h incubation
Luciferase
Analysis of luciferase activity
Primary naïve TH cells (Healthy donor)
± HD / HC serum 2.5%
+ αCD3ε, αCD28
+ TGF-β, IL-1β, IL-6, IL-21, IL-23
7 d incubation
TH17
Analysis by flow cytometry
c
Serum AhR activity (Luminescence a.u.)
HC VEH -7 -6
HD + AhRi [log M]
d
TH17 polarisation [%]
Ctrl HC HD
e
GFR categories [mL/min/1.73m²]
G1 (≥90)
G2 (60-89)
G3a (45-59)
G3b (30-44)
G4 or G5 (<29)
A1 (<30) A2 (30-300) A3 (>300)
Albuminuria categories [mg/mL]
Plasma IL-17A [mean NPX value]
f
Plasma IL-17A [NPX]
non-HFpEF HFpEF
eGFR < 60
n = 15981 n = 5497
g
eGFR < 60
Survival Probability
IL-17A <25th Perc
IL-17A 25th-75th Perc
IL-17A >75th Perc
log-rank: p = 0.010
Time [years]
At risk
<25th: 534 521 507 482 452 425 391 194
25th-75th: 1273 1236 1200 1135 1072 997 920 462
>75th: 978 949 912 859 810 750 669 315
h
IL-17A
Model 1 p < 0.0001
Model 2 p = 0.0129
Model 3 p = 0.0445
Hazard ratio (95% CI) for all-cause mortality
i
± HD / HC serum 10%
± AhRi
± αIL17A
24 h incubation
Human cardiac fibroblasts
Analysis by qPCR
j
IL17RA Relative mRNA expression
k
COL1A1 Relative mRNA expression
l
COL1A2 Relative mRNA expression
m
ACTA2 Relative mRNA expression
HC HD HD αIL17A HD AhRi